

Grid effect on spherical shallow water jets using continuous and discontinuous Galerkin methods

S. Marras*, M. A. Kopera, F. X. Giraldo

Department of Applied Mathematics, Naval Postgraduate School

*Correspondence to: 833 Dyer Road, Bldg. 232, Spanagel 249A, Monterey, CA 93943 U.S.A.
smarras1@nps.edu; fxgirald@nps.edu

Element-based Galerkin methods are not constrained by the logical structure of the computational grid. In this paper, the behavior of the continuous and discontinuous Galerkin solutions of the shallow water equations on the sphere is analyzed for three different grids of ubiquitous use in atmospheric modeling: (A) hexahedron (or cubed sphere), (B) reduced latitude-longitude, and (C) icosahedron. Conforming and nonconforming mesh configurations are adopted. The nonconforming grids are based on a quad-tree structure. The analysis is performed on the mid-latitude zonal flow problem suggested by Galewsky et al. [An initial-value problem for testing numerical models of the global shallow-water equation, *Tellus* 2004; 56A:429–440]. This test is sufficiently simple in its implementation, yet sufficiently complex to capture some important modes that arise on the global scales of real atmospheric dynamics. Because the inviscid solution on certain grids shows a high sensitivity to the resolution, the viscous counterpart of the governing equations are also solved and the results are compared. The study shows that not only the resolution, but the grid alignment with respect to the flow is important in order to obtain an accurate solution. This is especially true if the governing equations are not regularized by the addition of a sufficiently large, fully artificial, diffusion mechanism; we give a brief (not exhaustive) analysis of the effect of viscosity on the solution quality. The flexibility and accuracy of element-based Galerkin methods on general spherical geometries is illustrated; we particularly emphasize the excellent properties of the reduced Lat-Lon configuration in comparison with the cubed-sphere on the one hand, and with the more regular and uniform icosahedral grid on the other.

Key Words: Reduced Lat-Lon grids; Icosahedral Grid; Cubed-Sphere; Shallow Water Equations; Galerkin Methods; Spectral Element; Discontinuous Galerkin; Barotropic Jet; Galewsky Flow; Grid Generation on the Sphere; Transfinite Interpolation.

Received ...

1. Introduction

As computational power increases, meteorologists demand greater resolution from global atmospheric models utilizing spherical domains. Driven by the need to select the most proper computational grid on the sphere for the *Nonhydrostatic Unified Model of the Atmosphere* (NUMA) (Kelly and Giraldo 2012; Giraldo et al. 2013), in this paper we analyze the continuous Galerkin (or *spectral elements*

from now on) and discontinuous Galerkin (DG) solutions of the shallow water equations (SWE) on a set of common grids used in global circulation models (GCMs). Specifically, we study 1) the cubed-sphere (Hex) (Sadourny 1972), 2) the icosahedron (Ico) (Sadourny et al. 1968), and 3) a reduced latitude-longitude (Lat-Lon) geometry (Phillips 1957). Because SWE capture many of the essential features of GCMs while eliminating the vertical structure of the atmosphere, the results from this study will be directly applicable to the fully three-dimensional model NUMA.

The logically structured Hex and Lat-Lon grids can be advantageous for a finite difference based solver, and are generally usable by grid point methods such as finite

[†]Please ensure that you use the most up to date class file, available from the QJRMS Home Page at
[http://onlinelibrary.wiley.com/journal/10.1002/\(ISSN\)1477-870X](http://onlinelibrary.wiley.com/journal/10.1002/(ISSN)1477-870X)

| Report Documentation Page | | | Form Approved OMB No. 0704-0188 | |
|---|------------------------------------|---|--|---|
| <p>Public reporting burden for the collection of information is estimated to average 1 hour per response, including the time for reviewing instructions, searching existing data sources, gathering and maintaining the data needed, and completing and reviewing the collection of information. Send comments regarding this burden estimate or any other aspect of this collection of information, including suggestions for reducing this burden, to Washington Headquarters Services, Directorate for Information Operations and Reports, 1215 Jefferson Davis Highway, Suite 1204, Arlington VA 22202-4302. Respondents should be aware that notwithstanding any other provision of law, no person shall be subject to a penalty for failing to comply with a collection of information if it does not display a currently valid OMB control number.</p> | | | | |
| 1. REPORT DATE 2013 | 2. REPORT TYPE | 3. DATES COVERED 00-00-2013 to 00-00-2013 | | |
| 4. TITLE AND SUBTITLE Grid effect on spherical shallow water jets using continuous and discontinuous Galerkin methods | | | 5a. CONTRACT NUMBER | |
| | | | 5b. GRANT NUMBER | |
| | | | 5c. PROGRAM ELEMENT NUMBER | |
| 6. AUTHOR(S) | | | 5d. PROJECT NUMBER | |
| | | | 5e. TASK NUMBER | |
| | | | 5f. WORK UNIT NUMBER | |
| 7. PERFORMING ORGANIZATION NAME(S) AND ADDRESS(ES) Naval Postgraduate School, Department of Applied Mathematics, Monterey, CA, 93943 | | | 8. PERFORMING ORGANIZATION REPORT NUMBER | |
| 9. SPONSORING/MONITORING AGENCY NAME(S) AND ADDRESS(ES) | | | 10. SPONSOR/MONITOR'S ACRONYM(S) | |
| | | | 11. SPONSOR/MONITOR'S REPORT NUMBER(S) | |
| 12. DISTRIBUTION/AVAILABILITY STATEMENT Approved for public release; distribution unlimited | | | | |
| 13. SUPPLEMENTARY NOTES | | | | |
| 14. ABSTRACT | | | | |
| 15. SUBJECT TERMS | | | | |
| 16. SECURITY CLASSIFICATION OF: | | | 17. LIMITATION OF ABSTRACT Same as Report (SAR) | 18. NUMBER OF PAGES 16 |
| a. REPORT unclassified | b. ABSTRACT unclassified | c. THIS PAGE unclassified | | |

and spectral element (FE, SE), discontinuous Galerkin (DG), or finite volume (FV) methods. Furthermore, Lat-Lon is the standard discretization for GCMs based on spectral transform methods due to the fast Fourier transform operation along the longitude direction (Hogan *et al.* 1991). Icosahedral grids or, more generally, unstructured tri- and quad-based tessellations* of the sphere are geometrically flexible, but not all numerical methods are able to handle them. (A review of different grid generation techniques in atmospheric modeling can be found in the book by Behrens (2006).) Recently, different grids to be used with finite volume discretization techniques have been analyzed in, e.g., Qaddouri *et al.* (2012); Weller *et al.* (2012) or Peixoto and Barros (2013), with a review appearing in Staniforth and Thuburn (2012). In the context of Galerkin methods, however, not much analysis has been conducted with respect to the solution dependence on these computational grids. Rather, given a specific grid, we are likely to find a model that is developed around it and is optimized to minimize the error in a specific configuration. In the case of the solution of shallow water problems, examples of this approach are the works by Taylor *et al.* (1997) (SE on cubed-sphere), Lanser *et al.* (2000) (FV on a reduced Lat-Lon geometry), Giraldo (2001) (SE on the quad-based icosahedron), Giraldo *et al.* (2002) (DG on a triangle-based icosahedron), or Nair *et al.* (2007) (DG on the cubed sphere). One step forward in grid comparison was made by Giraldo and Warburton (2005) who compared different triangle-based unstructured grids amongst each other and, subsequently, against the cubed sphere. They concluded that the accuracy of the solution is clearly a function of the combination of the grid and the problem that is being solved, and it does not depend on either the numerical method or the grid alone. A comparison between dynamically adaptive and uniform meshes was performed by Müller *et al.* (2013) for triangle based discontinuous Galerkin methods.

In 2008, St-Cyr *et al.* compared two shallow water solvers based on spectral elements on the one hand, and finite volumes on the other (see St-Cyr *et al.* (2008)). The two models were designed to execute on different grids: a cubed-sphere (SE solver) and on a Lat-Lon grid (FV model). In their study, they assert that the spectral element method is unable to capture the solution at certain resolutions. In this paper we show that the inaccuracies that they encountered are not linked to the numerical method per se, but rather, to the unfortunate combination of the resolution and alignment of the mesh with respect to the dynamics that was being resolved in that specific study. We will confirm their conclusion that a coarse resolution is responsible for a wavenumber-4 signal that destroys the solution on the hexahedral grid; nevertheless, the simple change of grid will disproof the responsibility of SE and, rather, show that the instabilities are merely an undesired effect of the grid configuration.

This study is performed by solving the two nonlinear zonal flows proposed by Galewsky *et al.* (2004). At low resolution, the flows on the cubed-sphere and icosahedron completely diverge from the true solutions in the case of (i) the equilibrium, and (ii) the barotropic instability tests. As the resolution is increased, the effect of the irregular grid geometry is partially camouflaged and eventually disappears. In search of the coarsest allowable resolution to be used while still preserving accuracy, we added an artificial diffusion

with constant coefficient $\nu = 1 \times 10^5 \text{ m}^2 \text{ s}^{-1}$ as suggested by Galewsky *et al.* (2004). The positive effect of diffusion is clear for the low resolution results on the cubed-sphere and icosahedron; on the contrary, we will show how this is not completely true for the solution on the reduced Lat-Lon grid. It must be pointed out that the diffusion correction that was adopted is fully artificial and has no physical meaning. The sole reason for its use in this study is to be able to analyze the solution when the grid is not of sufficient resolution to properly resolve the flow. Partially based on this study, but mostly on the analysis made by practitioners in computational fluid dynamics for more than three decades, we strongly believe that simple Laplace operators (of any order) for stabilization purposes should be avoided for the sake of accuracy. If viscosity is indeed necessary, techniques similar to those described in Malm *et al.* (2013) or Marras *et al.* (2013b,a), among others, may be valuable options to consider for the solution of the shallow water and Euler equations. Research in this direction is still on-going; especially so in atmospheric applications.

Finally, to assess the ability of the algorithm to handle conforming and nonconforming grids with refinement, we complete the study by building six statically adapted grids. We constructed a fixed high-resolution grid core in the region where the zonal jet is most likely to develop, and coarsened the rest of the domain with a 1- and 2-level de-refinement approach to estimate the error when the total number of grid points is drastically reduced. The DG solution algorithm on the refined grids is based on the procedure by Kopera and Giraldo (2013) and references therein.

The paper is organized as follows. In Sec. 2, we report on the construction of high-order grids on the sphere. The model equations are described in Sec. 3 whereas the numerical method of solution is described in Sec. 4. We describe the tests and analyze the results in Sec. 5. We finally summarize our findings in Sec. 6.

2. High order grid generation on the sphere

Grid generation on the sphere is a relatively easy task. However, finding the grid that can suit different numerical methods is not. Because element-based Galerkin methods have the advantage of being flexible with respect to the grid, we analyze how different meshes on the sphere can affect the spectral element and discontinuous Galerkin solution of the shallow water equations.

A standard approach to high order grid generation is based on the construction of a linear grid first (i.e. a grid with straight edges whose extrema are the only points that lie on the geometry), and then to populate it with the high order internal points. The population step is performed element-wise in the logical space obtained by a proper projection from the physical space. Once the higher order grid points have been built on the plane, a backward projection onto the physical geometry moves the new high order elements onto the sphere. This process is such that the high order elements approximate the surface faithfully. The projection from the sphere to the logical space may differ from grid to grid. The gnomonic projection by Ronchi *et al.* (1996) was used to build the high order grids. In what follows, we describe how the RLL, Hex, and Ico grids were constructed.

2.1. Reduced Lat-Lon grid (RLL)

Since the effort of Phillips (1957) to reduce the singularity problem at the poles of a global latitude-longitude grid, different types of reduced Lat-Lon grid (RLL from now

*The keywords *grid*, *mesh*, and *tessellation* will be used interchangeably throughout the paper.

on) have been used. Partially based on the composite methods of Starius (1977) and Browning *et al.* (1989), Lanser *et al.* (2000) solved the shallow water equations on a Lat-Lon grid away from the poles combined with a stereographic grid at the poles. In this paper, we build and test a modified, high order version of Lanser's grids. The interfaces between the reduced Lat-Lon area and the polar caps are obtained by a transfinite interpolation (TFI) (Gordon and Hall 1973; Eriksson 1984). The way this is done will be described shortly. To build the RLL grid we used a multiblock approach (see, e.g., Thompson (1987)) that consists of building a set of independent, simply connected surface grids that are eventually patched together to form the global mesh. The main RLL region and the polar caps are the first blocks to be built. The main Lat-Lon region is composed of four faces obtained from the master face $\gamma_1 = [-\pi/4 \leq \lambda \leq \pi/4] \times [\varphi_{min} \leq \varphi \leq \varphi_{max}]$ and from its rotation with respect to the z -axis of the sphere. The variables λ and φ indicate longitude and latitude. The RLL band in the northern and southern hemispheres is delimited by φ_{min} and φ_{max} . The rotation matrix from γ_1 to the three remaining faces $\gamma_2, \gamma_3, \gamma_4$ is obtained by the combined effect of a translation on the xy -plane and a rotation around the z -axis; this transformation is given by

$$[T] = \begin{bmatrix} 1 & 0 & 0 & 0 \\ 0 & 1 & 0 & 0 \\ 0 & 0 & 1 & 0 \\ l & m & n & 1 \end{bmatrix} \begin{bmatrix} \cos(\lambda_{rot}) & \sin(\lambda_{rot}) & 0 & 0 \\ -\sin(\lambda_{rot}) & \cos(\lambda_{rot}) & 0 & 0 \\ 0 & 0 & 1 & 0 \\ 0 & 0 & 0 & 1 \end{bmatrix}.$$

The first matrix produces a translation $[l \ m \ n] = [-1 \ -1 \ -1]$ along (x, y, z) and is followed by the rotations $\lambda_{rot,i=2,3,4} = (\pi/2, \pi, 3\pi/2)$ given by the action of the second matrix. The coordinates on each rotated planar face are simply a function of $(x, y, z)_{\gamma_i}$ and are computed as

$$[x \ y \ z \ 1]_{\gamma_i} = [x \ y \ z \ 1]_{\gamma_1}[T], \quad i = 2, 3, 4. \quad (1)$$

Once rotated, each gridded face is projected onto the sphere. The polar caps are built in the same way, except that the starting point is the square plane defined within the region $\gamma_9 = [-\pi/4 \leq \lambda \leq \pi/4] \times [-\pi/4 \leq \varphi \leq \pi/4]$. At this point we have a linear grid made of 6 disjoint regular patches. The top view of this is shown in Fig. 1. Eight new surfaces must now be built to fill the ungridded gaps.

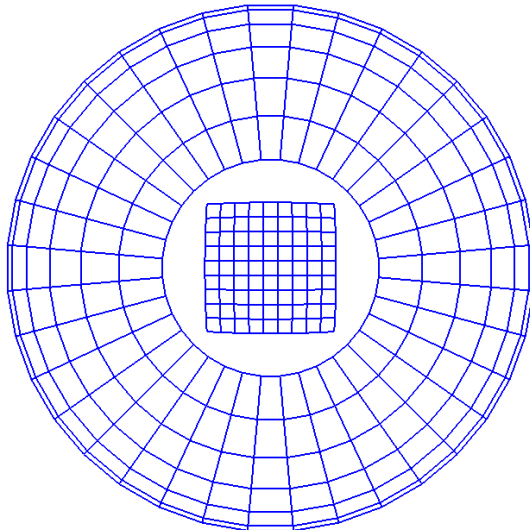


Figure 1. Linear grid. Top x - y view of the disjoint lateral Lat-Lon and top patches in the multi-block RLL grid. TFI is used to connect them together through an interface surface grid.

To build each interface surface by TFI we need information from its four boundary edges. With reference to the schematic of Fig. 2, the region delimited by edges 1, 2, 3, 4 is built in two steps: (a) given the (λ, φ) coordinates of the corner points 1-2-3-4, build edges 3 and 4 and subdivide them into $N_{elat,int}$ 1D linear elements, where $N_{elat,int}$ is the user-defined number of elements along the latitude direction in the interface region; (b) compute the grid points in the interior of the patch using the planar and linear transfinite interpolation defined by the Boolean sum

$$\mathbf{X}(\hat{\xi}, \hat{\eta}) = \mathbf{U} + \mathbf{V} - \mathbf{U} \otimes \mathbf{V}, \quad (2)$$

where, given the arrays $\hat{\xi} = 0, \dots, 1$ and $\hat{\eta} = 0, \dots, 1$ in computational space along the local (\hat{u}, \hat{v}) directions, the univariate interpolations and tensor products (\otimes) are computed as

$$\begin{aligned} \mathbf{U}(\hat{\xi}, \hat{\eta}) &= (1 - \hat{\xi})\mathbf{X}(0, \hat{\eta}) + \hat{\xi}\mathbf{X}(1, \hat{\eta}) \\ \mathbf{V}(\hat{\xi}, \hat{\eta}) &= (1 - \hat{\eta})\mathbf{X}(\hat{\xi}, 0) + \hat{\eta}\mathbf{X}(\hat{\xi}, 1) \\ \mathbf{U} \otimes \mathbf{V}(\hat{\xi}, \hat{\eta}) &= (1 - \hat{\xi})(1 - \hat{\eta})\mathbf{X}(0, 0) + (1 - \hat{\xi})\hat{\eta}\mathbf{X}(0, 1) \\ &\quad - (1 - \hat{\eta})\hat{\xi}\mathbf{X}(1, 0) - \hat{\xi}\hat{\eta}\mathbf{X}(1, 1). \end{aligned} \quad (3)$$

In Equations (2), \mathbf{X} is the array of the (λ, φ) coordinates of the grid points in the interior of the surface, given the known values of the surface boundary edges stored in $\mathbf{X}(0, \hat{\eta}), \mathbf{X}(1, \hat{\eta}), \mathbf{X}(\hat{\xi}, 0), \mathbf{X}(\hat{\xi}, 1)$, and corners $\mathbf{X}(0, 0), \mathbf{X}(1, 1), \mathbf{X}(1, 0), \mathbf{X}(0, 1)$.

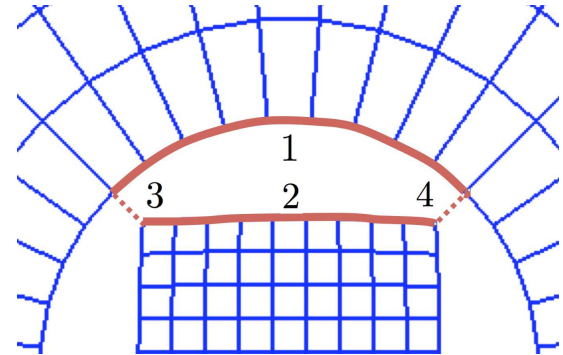


Figure 2. Detail of one interface patch in the northern hemisphere.

The high-order Legendre-Gauss-Lobatto (LGL) points are added to the linear grid by projecting the linear elements onto the auxiliary gnomonic space (on the plane), and back-projecting the new high order quads onto the sphere. The total number of elements N_e and grid points N_p of the high order conforming grid are given by:

$$N_e = \begin{array}{ll} 4N_{elon}N_{elat} & \text{Lateral Lat-Lon} \\ +2N_{elon}N_{elon} & \text{Polar caps} \\ +8N_{elon}N_{elat,int} & \text{Transition zone,} \end{array} \quad (4)$$

and

$$N_p = \begin{array}{ll} 4N_{elon}p(N_{elat}p + 1) & \text{Lateral} \\ +2(N_{elon}p + 1)(N_{elat}p + 1) & \text{Polar} \\ +2(4N_{elon}p(N_{elat,int}p + 1) - 8N_{elon}p) & \text{Transition.} \end{array} \quad (5)$$

In (4) and (5), N_{elon} is the number of elements of order N along the longitude direction of one face in the main Lat-Lon band that, by construction, coincides with the number

of longitude elements in the interface and polar regions. N_{elat} and $N_{elat,int}$ are, respectively, the number of latitude elements of the Lat-Lon region and of the interface patches. The number of latitude elements in the polar caps is also given by N_{elon} .

Fig. 3 shows an example of a high-order conforming RLL tessellation.

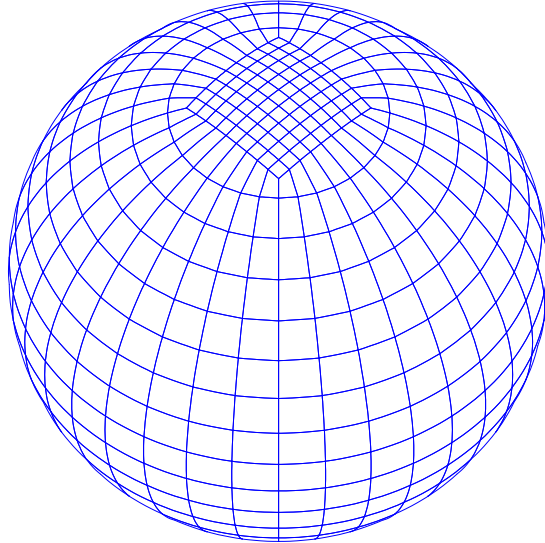


Figure 3. Conforming RLL grid.

2.2. Cubed sphere (or Hexahedral)

The cubed sphere (see, e.g. [Ronchi et al. \(1996\)](#); [Taylor et al. \(1997, 2013\)](#)) is derived from the projection of a cube onto the sphere. As such, it consists of 6 faces that are then subdivided into as many elements as necessary. Like RLL, we built this grid in a multi-block fashion by going through the same steps described above. The fundamental difference is that the hexahedral grid (Hex, from now on) has only 6 faces and they are all equal. An example is shown in Fig. 4. The internal LGL points are omitted for simplicity. By construction, the elements that are furthest from the center of each face are smaller than those at the face center; in addition, their distorted shape prove to be a concern when the resolution is not sufficiently high. We will discuss this issue shortly.

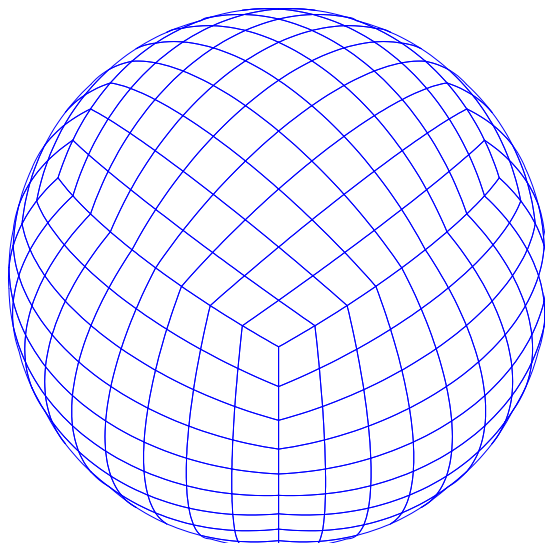


Figure 4. Conforming Hex grid.

2.3. Quad-based icosahedral grid

The quad-based icosahedral grid of order N is derived from an initial icosahedron of 20 triangles. For better properties of the high order grid, every triangle is mapped onto a gnomonic space by the transformation formulas ([Giraldo \(2001\)](#))

$$x = r \tan \lambda', \quad (6a)$$

$$y = r \tan \varphi' \sec \lambda', \quad (6b)$$

where r is the radius of the sphere and, given the centroids (λ_c, φ_c) of each triangle, we define

$$\lambda' = \text{atan} \left[\frac{\cos \varphi \sin(\lambda - \lambda_c)}{\cos \varphi_c \sin \varphi + \cos \varphi_c \cos \varphi \cos(\lambda - \lambda_c)} \right], \quad (7a)$$

$$\varphi' = \text{asin} [\cos \varphi_c \sin \varphi - \sin \varphi_c \cos \varphi \cos(\lambda - \lambda_c)]. \quad (7b)$$

After mapping, the triangles are subdivided into smaller ones by a Lagrange polynomial of order n_I .

The number of quadrilateral elements and grid points of the final grid are then given by

$$N_p = 6(N_p^T - 2)p^2 + 2$$

$$N_e = 6(N_p^T - 2)$$

where the number of points N_p^T of the original triangular grid can be found in [Giraldo \(2001\)](#).

Fig. 5 shows the 8th order icosahedral grid. As for the previous cases, the elements are curved and lie on the spherical surface.

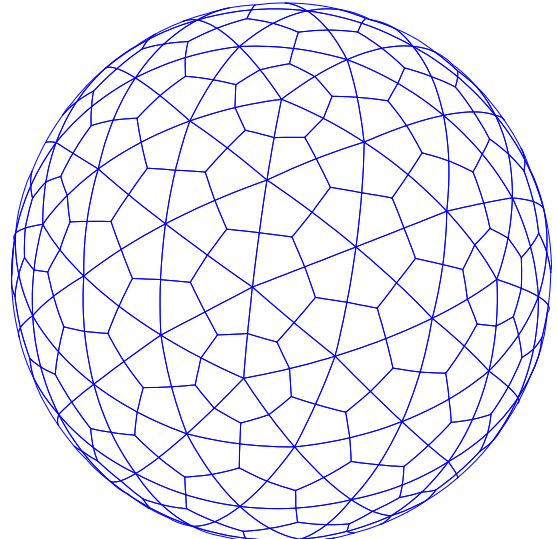


Figure 5. Conforming Ico grid.

3. Shallow water equations on the sphere

3.1. Equations of motion

Under the assumption of a shallow depth, the motion of an incompressible fluid may be described by the non-linear shallow water equations. The shallow water assumption holds as long as the characteristic horizontal extension of the fluid is much larger than its depth. The vector representation of the shallow-water equations in the Cartesian coordinates $\mathbf{x} = (x, y, z)$ is given, in flux form, by

$$\frac{\partial \phi}{\partial t} + \nabla \cdot (\phi \mathbf{u}) = 0 \quad (8a)$$

$$\frac{\partial \phi \mathbf{u}}{\partial t} + \nabla \cdot (\phi \mathbf{u} \otimes \mathbf{u}) = -\phi \nabla \phi - f(\mathbf{x} \times \phi \mathbf{u}) + \mu \mathbf{x} + \delta \nu \nabla^2(\phi \mathbf{u}) \quad (8b)$$

where $\phi = gh$ is the geopotential height (g and h are the modulus of the acceleration of gravity and the vertical height of the fluid), $\nu \nabla^2$ is the artificial viscosity term of viscous coefficient $\nu = 1 \times 10^5 \text{ m}^2 \text{ s}^{-1}$ that is de-activated by the switch $\delta = 0$, $\mathbf{u} = (u, v, w)^T$ is the velocity vector, $\nabla = (\partial_x, \partial_y, \partial_z)^T$, and $f = 2\omega z/r^2$ is the Coriolis parameter with Earth's angular velocity $\omega = 7.292 \times 10^{-5} \text{ s}^{-1}$ and mean radius $r = 6.37122 \times 10^6 \text{ m}$. For the fluid particles to remain on the spherical surface defined in 3D cartesian space, the normal component of the velocity field with respect to the sphere is removed by the term $\mu \mathbf{x}$ in the momentum equation, where μ is the Lagrange multiplier that serves this purpose. The construction of the Lagrange multiplier is described in Sec. 3.2.

3.2. Forcing the fluid onto the sphere by a Lagrange multiplier

We used the approach of Coté (1988). Specifically, at the end of every time step $n+1$, the momentum of the flow must be corrected for the particles to remain on the sphere. If c and u denote the constrained and unconstrained values of $\phi \mathbf{u}$, the new momentum is corrected according to

$$(\phi \mathbf{u})_c^{n+1} = (\phi \mathbf{u})_u^{n+1} + \mu \mathbf{x}. \quad (9)$$

For the fluid to remain on the sphere, the condition $\mathbf{u} \cdot \mathbf{x} = 0$ must hold (i.e., the velocity field and the position vector must be orthogonal), hence implying that $\phi \mathbf{u}_c \cdot \mathbf{x} = 0$ in equation (9). For this to be true, the value of the multiplier is found to be $\mu = -\phi \mathbf{u}_u^{n+1} \cdot \mathbf{x}/r^2$.

The Galerkin discretization of (8) is described in the next section.

4. Numerical method

4.1. Spectral elements and discontinuous Galerkin approximation

To solve the shallow water equations by element-based Galerkin methods on a domain Ω , we proceed by defining the weak form of (8) that we first write in compact form as

$$\frac{\partial \mathbf{q}}{\partial t} + \nabla \cdot \mathbf{F}(\mathbf{q}) = \mathbf{S}(\mathbf{q}), \quad (10)$$

where $\mathbf{q} = [\phi, \phi \mathbf{u}]^T$ is the array of the solution variables, and \mathbf{F} and \mathbf{S} are the flux and source terms that can be easily identified in the equations (8) above. Given a basis function ψ that belongs to the Sobolev space H^1 in the case of spectral elements, and to L^2 in the case of DG, the weak form of (10) is given by the integral

$$\int_{\Omega} \psi \left[\frac{\partial \mathbf{q}}{\partial t} + \nabla \cdot \mathbf{F}(\mathbf{q}) - \mathbf{S}(\mathbf{q}) \right] d\Omega = 0, \quad (11)$$

that, after integration by parts of the flux, becomes

$$\begin{aligned} \int_{\Omega} \psi \frac{\partial \mathbf{q}}{\partial t} d\Omega - \int_{\Omega} \nabla \psi \cdot \mathbf{F}(\mathbf{q}) d\Omega - \int_{\Omega} \psi \mathbf{S}(\mathbf{q}) d\Omega + \\ \int_{\Gamma} \psi \mathbf{n} \cdot \check{\mathbf{F}}(\mathbf{q}) d\Gamma = 0, \end{aligned} \quad (12)$$

where $\check{\mathbf{F}}(\mathbf{q})$ indicates the numerical flux of the advection and diffusion terms across the boundary Γ . In the case of spectral elements, where the basis functions are continuous across neighboring elements, and given that the problem is solved on a closed manifold, the boundary integral \int_{Γ} vanishes. On the other hand, in the case of the DG method, the boundary integral remains because of the non-zero inter-element fluxes. Furthermore, the surface integrals for DG are defined element-wise over Ω_e rather than globally over Ω . This makes Equations (11) and (12) a system of N_e equations that are coupled via the flux of Equation (12). Both options are available within the same code used for this study and both methods share most of the numerical machinery.

The integrals above are solved element-wise on the discrete polyhedral approximation Ω^h . The discrete domain Ω^h is defined by the union of N_e non-overlapping quadrilateral elements Ω_e^h . For every element we define a bijective transformation $\mathcal{F}_{\Omega_e^h} : (x, y, z) \rightarrow (\xi, \eta, \zeta)$ that maps the physical coordinate system, (x, y, z) to the reference system (ξ, η, ζ) and is such that the reference element $\hat{\Omega}_e^h(\xi, \eta) = [-1, 1] \times [-1, 1]$ lies on the spherical surface. ζ is thus the spherical radius vector whose discrete values identify a spherical shell (e.g. $\zeta = 1$ is the sphere of unit radius.)

The Jacobian matrix of the transformation has components $J^i = \partial_{\xi} \mathcal{F}^i$ and determinant $|J| = \partial_{\zeta} \mathbf{x} \cdot \mathbf{G}$, where $\mathbf{G} = \partial_{\xi} \mathbf{x} \times \partial_{\eta} \mathbf{x}$ is the surface conforming component of the transformation (Song and Wolf 1999; Giraldo 2001).

Given the definition of the reference element, the element-wise solution can be approximated by the expansion

$$q_N(\mathbf{x}, t)|_{\Omega_e} = \sum_{k=1}^{(N+1)^2} \psi_k(\mathcal{F}_{\Omega_e}^{-1}(\mathbf{x})) q_N(\mathbf{x}_k, t), \quad e = 1, \dots, N_e \quad (13)$$

where $(N+1)^2$ is the number of collocation points within the element of order N , and ψ_k are the interpolation polynomials evaluated at point k . The basis functions ψ_k are constructed as the tensor product of the one-dimensional functions $h_i(\xi(\mathbf{x}))$ and $h_j(\eta(\mathbf{x}))$ as:

$$\psi_k = h_i(\xi(\mathbf{x})) \otimes h_j(\eta(\mathbf{x})),$$

$\forall i, j = 0, \dots, N$. $h_i(\xi(\mathbf{x}))$ and $h_j(\eta(\mathbf{x}))$ are the basis functions associated with the N LGL points ξ_i and η_j , respectively, given by the roots of

$$(1 - \xi^2) P'_N(\xi) = 0,$$

where $P'_N(\xi)$ is the derivative of the N^{th} -order Legendre polynomial. Given these definitions, the one-dimensional Lagrange polynomials $h_i(\xi)$ are

$$h_i(\xi) = -\frac{1}{N(N+1)} \frac{(1 - \xi^2) P'_N(\xi)}{(\xi - \xi_i) P_N(\xi_i)}.$$

The functions $h_j(\eta)$ are computed in the same way.

The same expansion above is used to construct the derivatives. We write:

$$\begin{aligned} \frac{\partial q_N(\mathbf{x}, t)}{\partial t}|_{\Omega_e} &= \sum_{k=1}^{(N+1)^2} \psi_k(\mathcal{F}_{\Omega_e}^{-1}(\mathbf{x})) \frac{\partial q_N(\mathbf{x}_k, t)}{\partial t}, \\ \frac{\partial q_N(\mathbf{x}, t)}{\partial \mathbf{x}}|_{\Omega_e} &= \sum_{k=1}^{(N+1)^2} \frac{\partial \psi_k(\mathcal{F}_{\Omega_e}^{-1}(\mathbf{x}))}{\partial \mathbf{x}} q_N(\mathbf{x}_k, t). \end{aligned} \quad (14)$$

The integrals are computed by numerical quadrature on the reference element as follows:

$$\int_{\Omega_e^h} \mathbf{q}(\mathbf{x}, t) d\mathbf{x} = \int_{\hat{\Omega}_e^h} \mathbf{q}(\xi, t) |\mathbf{J}(\xi)| d\xi \approx \sum_{i,j=1}^{N_{gl}} q(\xi_i, \eta_j, t) |\mathbf{J}(\xi_i, \eta_j)| \omega_i^\xi \omega_j^\eta, \quad (15)$$

where the Gaussian quadrature weights $\omega_{i,j}$ are computed as

$$\omega_{i,j} = \frac{2}{N(N+1)} \left(\frac{1}{P_N(\xi_i, \eta_j)} \right)^2.$$

In the case of spectral elements, the substitution of the expansions (13,14) into the weak form (12) yields the semi-discrete (in space) matrix problem

$$\frac{\partial \mathbf{q}}{\partial t} = \widehat{\mathbf{D}}^\tau \mathbf{F}(\mathbf{q}) + \mathbf{S}(\mathbf{q}) \quad (16)$$

where, for the global mass and differentiation matrices, M and \mathbf{D} , we have that $\widehat{\mathbf{D}} = M^{-1}\mathbf{D}$. The global matrices are obtained from their local counterparts, M^e and \mathbf{D}^e , by means of the direct stiffness summation operation that maps the local degrees of freedom of an element Ω_e^h to the corresponding global degrees of freedom in Ω^h , and adds the element values in the global system. By construction, M is diagonal (assuming inexact integration), with an obvious advantage if explicit time integration is used.

Concerning the discontinuous Galerkin approximation, the problem at hand is solved only locally, and unlike the case of spectral elements, the flux integral in Equation (12) must be discretized as well. The element-wise counterpart of the matrix problem (16) is then written as:

$$\frac{\partial \mathbf{q}^e}{\partial t} = -(\widehat{\mathbf{M}}^{s,e})^\tau \check{\mathbf{F}}(\mathbf{q}^e) + (\widehat{\mathbf{D}}^e)^\tau \mathbf{F}(\mathbf{q}^e) + \mathbf{S}(\mathbf{q}^e), \quad (17)$$

where we obtain $\widehat{\mathbf{M}}^{s,e} = (M^e)^{-1} \mathbf{M}^{s,e}$ from the element boundary matrix, $\mathbf{M}^{s,e}$, and the element mass matrix, M^e . Out of various possible choices for the definition of the numerical flux $\check{\mathbf{F}}(\mathbf{q})$ in Equation (17), we selected the Rusanov flux that, for the inviscid part of the flux, is constructed as

$$\check{\mathbf{F}}(\mathbf{q}) = \frac{1}{2} [\mathbf{F}_N(\mathbf{q}_N^L) + \mathbf{F}_N(\mathbf{q}_N^R) - |\lambda|(\mathbf{q}_N^R - \mathbf{q}_N^L)\mathbf{n}], \quad (18)$$

where $|\lambda| = |\mathbf{n} \cdot \mathbf{u}| + \sqrt{\phi}$ is the maximum wave speed of the shallow water equations. By identifying an intrinsic tangential direction in each inter-element boundary edge, \mathbf{q}_N^L and \mathbf{q}_N^R denote the solution in the left (L) and right (R) elements, respectively. For a detailed description of the DG algorithm that was used for this study, the reader is referred to Kopera and Giraldo (2013).

4.2. Time integration

The solution of the systems of ordinary differential equations (16,17) is advanced in time by a third-order strong stability preserving Runge-Kutta method (SSP-RK3) (Cockburn and Shu 2001; Spiteri and Ruuth 2002) that yields the solution at step $n+1$ as

$$\mathbf{q}^k = \alpha_0^k \mathbf{q}^n + \alpha_1^k \mathbf{q}^{k-1} + \beta^k \Delta t R(\mathbf{q}^{k-1}), \text{ for } k = 1, \dots, K,$$

where $R(\mathbf{q})$ indicates the right-hand sides of equations (16,17), K is the number of stages of the RK method, and $\mathbf{q}^0 = \mathbf{q}^n, \mathbf{q}^K = \mathbf{q}^{n+1}$. All the computations were executed with a maximum Courant-Friedrichs-Lowy number (CFL, Courant et al. (1967)) approximately 0.5. This value ensures the stability of the scheme given that the time step Δt is such that

$$\Delta t \leq CFL \min_{\mathbf{x} \in \Omega^h} [|\mathbf{u} \cdot \boldsymbol{\chi}| + \phi \sqrt{\boldsymbol{\chi} \cdot \boldsymbol{\chi}}]^{-1}.$$

The local grid distortion, $\boldsymbol{\chi}$, is defined as the vector

$$\boldsymbol{\chi} = \left(\frac{|\xi_x|}{\Delta\xi} + \frac{|\eta_x|}{\Delta\eta}, \frac{|\xi_y|}{\Delta\xi} + \frac{|\eta_y|}{\Delta\eta}, \frac{|\xi_z|}{\Delta\xi} + \frac{|\eta_z|}{\Delta\eta} \right)$$

where $\Delta\xi$ and $\Delta\eta$ are the local average grid size across the surface.

In the absence of dissipation (e.g., artificial diffusion), the high order numerical solution of advective problems may be characterized by spurious high frequency modes. To preserve full stability, along with respecting the CFL condition, we applied the standard spatial Boyd-Vandeven filter (Boyd 1996) at every time step. The filter constant was chosen to reduce by 5% the highest modes only.

5. Tests

To evaluate the behaviour of the solution on the three grid families, the highly nonlinear zonal dynamics test by Galewsky et al. (2004) was run at different resolutions using elements of order 8. Based on the analysis by Gaberšek et al. (2012), 8 is the order that we are likely to use when running operational (weather prediction) simulations with NUMA. The test consists of (i) an unperturbed mid-latitude zonal jet on top of a geostrophically balanced geopotential height, and of (ii) its perturbed counterpart where the perturbation is triggered by a bump in the geopotential. In either case, the initial zonal velocity and height are a function of the latitude φ (measured in radians unless otherwise specified) as

$$u(\varphi) = \begin{cases} 0 & \text{if } \varphi \leq \varphi_0 \text{ or } \varphi \geq \varphi_1 \\ \frac{u_{\max}}{e_n} \exp \left[\frac{1}{(\varphi - \varphi_0)(\varphi - \varphi_1)} \right] & \text{if } \varphi_0 < \varphi < \varphi_1, \end{cases} \quad (19)$$

where $u_{\max} = 80 \text{ m s}^{-1}$ is the maximum zonal velocity and $(\varphi_0, \varphi_1) = (\pi/7, \pi/2 - \varphi_0)$ are the lowest and highest latitudes that delimit the jet. At the jet mid-point, where $\varphi = \pi/4$, the non-dimensional parameter $e_n = \exp[-4/(\varphi_1 - \varphi_0)^2]$ normalizes the jet magnitude to u_{\max} . From the initial zonal flow given by (19), the height $g\phi$ is found by solving

$$g\phi(\varphi) = g\phi_0 - \int^{\varphi} r u(\varphi') \left[f + u(\varphi') \frac{\tan(\varphi')}{r} \right] d\varphi', \quad (20)$$

where the integral on the right-hand side is computed by numerical quadrature. As in the reference, φ_0 is chosen to give a global mean layer depth of 10 km. The height perturbation of test (ii) is the bump whose shape is given by

$$\phi'(\lambda, \varphi) = \hat{\phi} \cos(\varphi) \exp[-\lambda^2/\alpha^2] \exp[-(\varphi_2 - \varphi_1)^2/\beta^2] \quad \text{for } -\pi < \lambda < \pi, \quad (21)$$

where λ is the longitude, $\hat{\phi} = 120\text{ m}$, $\varphi_2 = \pi/4$, $\alpha = 1/3$ and $\beta = 1/15$. The definition of this bump is such that the perturbation is forced to zero at the poles.

The flows in (i) and (ii) are simulated along a time span of 144 hours. In the absence of any perturbation, the balanced field and zonal flow are expected to maintain their initial state indefinitely. The analytical initial field is used to compute the L_2 error norms of the numerical solutions as time evolves.

Although its solution seems trivial, this test is especially demanding for a shallow water model because of the large sensitivity of the solution to the grid resolution and geometry. Unlike other tests that may be more forgiving in this respect (e.g. the steady-state nonlinear zonal geostrophic flow by Williamson *et al.* (1992)), when the grid is not sufficiently fine, grid related oscillations may spoil the equilibrium with devastating consequences. This is clearly visible in Fig. 6, where the initially unperturbed and balanced zonal flow completely loses its initial state when the test is executed on the low resolution hexahedral and icosahedral grids. All the runs were executed at the equivalent resolutions $\Delta\lambda \approx \Delta\varphi = \{0.625^\circ, 1.25^\circ, 2.5^\circ, 5.0^\circ\}$ and for a varying number of grid points $N_p = \{12000, 25000, 50000, 100000\}$. The reason for the two sets of runs will be clarified in *Remark 1*.

Below, the keywords *Equilibrium* and *Perturbed jet* are used to identify, respectively, problems (i) and (ii).

Remark 1: equivalent resolutions A few words are in order regarding the issue of *equivalent resolution* when grids of a very different nature are compared against each other. In the case of spectral elements that rely on LGL nodes, the distance between two consecutive grid points changes within the same element. Because of this, the equivalent angular resolution along a latitude circle subdivided into $N_{e,\lambda}$ elements of order N is $2\pi/(N_{e,\lambda}N)$. Given this definition, we add that two resolutions are approximately equivalent when, within the region of major interest (e.g., where the dynamics is most likely to develop from a certain initial state), the size of the angular resolution of two different grids are comparable. In other words, when we say that the resolution is, e.g., $\Delta\lambda = 0.625^\circ$, it means that the mean angular distance between two meridians in the proximity of the jet measures 0.625° . This definition makes the measurement on the icosahedral grid not straightforward because of the irregular orientation of the elements. To obviate this problem, the error norms in the analysis below are also compared with respect to the total number of grid points.

5.1. Equilibrium

Fig. 6 shows the vorticity field Λ after 6 days for the unperturbed jet problem on the three different conforming grid types (rows) and $N_p = \{25000, 50000, 100000\}$ grid points (from left to right). For two out of the three grid geometries, the effect of the misalignment is still important for as many as 25000 grid points, which approximately corresponds to an equivalent resolution $\Delta\varphi = 1^\circ$ on the cubed-sphere. The solution on the RLL grid can maintain the jet with approximately 80% fewer grid points than the hexahedral grid and 50% fewer than the icosahedral grid. This is not reason enough to draw conclusions on the superiority of the RLL grid; rather, it should only suggest that, unless a sufficiently high resolution is used with grids

Table 1. *Equilibrium*. Normalized L_2 error of (ϕ, u_s, v_s) at day 6 using CG. The error is computed with respect to the analytical initial fields given by equations (19) and (20), and is reported against the total number of grid points.

| CG, L_2 | | | | |
|------------|----------|----------|----------|----------|
| N points | 100000 | 50000 | 25000 | 12000 |
| RLL | | | | |
| ϕ | 4.878e-8 | 1.802e-7 | 2.011e-5 | 1.466e-4 |
| u_s | 5.910e-5 | 1.586e-4 | 5.162e-3 | 2.701e-2 |
| v_s | 5.910e-5 | 1.586e-4 | 5.167e-3 | 2.706e-2 |
| Hex | | | | |
| ϕ | 6.099e-5 | 4.896e-4 | 5.440e-3 | 5.460e-3 |
| u_s | 6.679e-3 | 5.346e-2 | 5.458e-1 | 5.059e-1 |
| v_s | 6.679e-3 | 5.346e-2 | 5.458e-1 | 5.059e-1 |
| Ico | | | | |
| ϕ | 2.230e-5 | 2.593e-4 | 1.057e-2 | 1.263e-2 |
| u_s | 2.040e-3 | 2.313e-2 | 8.035e-1 | 9.163e-1 |
| v_s | 2.040e-3 | 2.313e-2 | 8.035e-1 | 9.163e-1 |

Table 2. *Equilibrium*. As table 1, but the error is reported against the equivalent resolution $\Delta\lambda$.

| CG, L_2 | | | | |
|-----------|----------|----------|----------|----------|
| RLL | 0.625° | 1.25° | 2.5° | 5.0° |
| N points | 180000 | 49000 | 16000 | 3000 |
| ϕ | 1.377e-8 | 5.017e-7 | 1.106e-4 | 2.056e-3 |
| u_s | 2.185e-5 | 3.167e-4 | 2.553e-2 | 4.694e-1 |
| v_s | 2.185e-5 | 3.167e-4 | 2.555e-2 | 4.694e-1 |
| Hex | 0.625° | 1.25° | 2.5° | 5.0° |
| N points | 124000 | 31000 | 9600 | 1500 |
| ϕ | 5.109e-5 | 4.721e-3 | 6.336e-3 | 1.038e-2 |
| u_s | 5.601e-3 | 4.709e-1 | 4.832e-1 | 6.918e-1 |
| v_s | 5.601e-3 | 4.709e-1 | 4.832e-1 | 6.918e-1 |

that are not aligned with the characteristic flow (which is likely to be the case in realistic simulations), we should not trust the solution with high fidelity.

In Tables 1 and 2 we report the normalized L_2 error norms of the geopotential height and zonal velocity against the number of grid points and, respectively, the equivalent resolution $\Delta\lambda$. These errors were computed using spectral elements on conforming grids; from here on, we shall refer to spectral elements as Continuous Galerkin (CG) to distinguish it from the discontinuous Galerkin (DG) method.

We mentioned above that the structure of the icosahedral grid is somewhat irregular and it is hence not straightforward to find a direct relationship between the number of grid points and the equivalent resolution. For this reason, we report the errors computed on the Ico grid in Table 3 against the equivalent resolutions and against the subdivision parameters [N6 N5 N4 N3 N2 N1] that are defined by the user to construct the grid. We plot the errors of Tables 1–3 in Figs. 7 and 8.

Let us focus on the curves with continuous lines as they trace the error on the uniform conforming grids. The conclusions drawn from the vorticity contours of Fig. 6 are confirmed by these error estimates. Furthermore, from Fig. 8 it is interesting to see that the L_2 error of the Hex solution reaches its peak value at $\Delta\lambda \approx 1.25^\circ$. This leaves very little room for resolution options when the cubed-sphere is used without viscosity. The results reported so far were computed with CG on conforming grids. However, we also ran the same tests using DG on every grid. As expected, the errors are practically identical to those obtained by CG; the solution accuracy for CG and DG should be identical because the

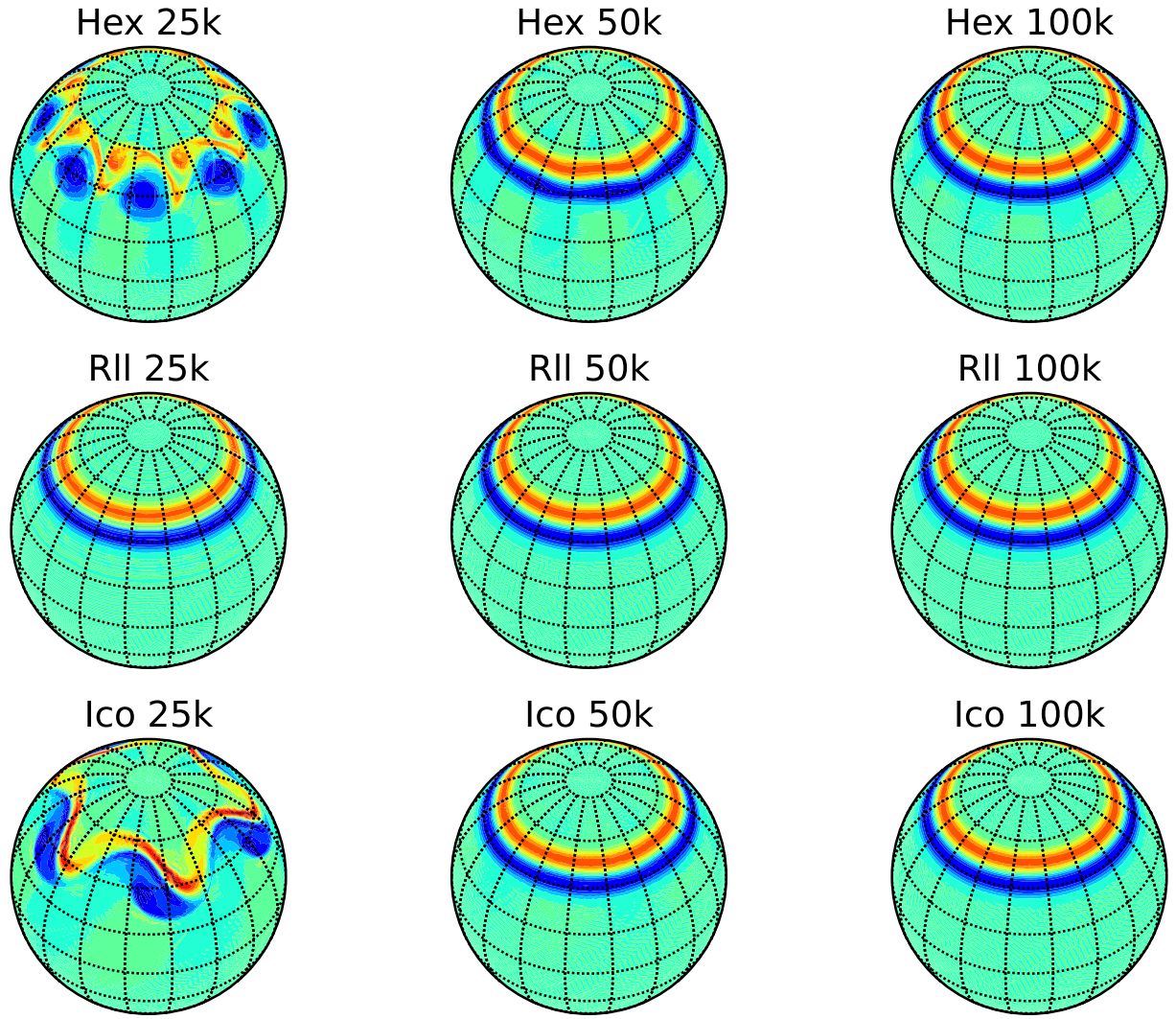


Figure 6. Equilibrium: Vorticity field ($\times 10^{-5} \text{ s}^{-1}$) after 6 days. The solutions on the hexahedral (top row), on the RLL (middle), and on the icosahedral grids (bottom row) are plotted for 25000, 50000, and 100000 grid points (from left to right). The color scale ranges between $-12 \times 10^{-5} \text{ s}^{-1}$ (dark blue) and $16 \times 10^{-5} \text{ s}^{-1}$.

Table 3. *Equilibrium*. As table 2, but on the icosahedron. Because of the geometrical structure of the icosahedron, the correspondence between the equivalent resolution and the number of subdivision indicated by $N6, \dots, N1$ is not as straightforward as it is for Hex and RLL.

| Geometry | $N6$ | $N5$ | $N4$ | $N3$ | $N2$ | $N1$ |
|-----------------------------|---------------|----------|--------------|----------|-------------|-------------|
| Approximate $\Delta\lambda$ | 0.625° | | 1.25° | | 2.5° | 5.0° |
| ϕ | 5.064e-6 | 2.299e-5 | 2.593e-4 | 6.157e-3 | 1.261e-2 | 1.033e-2 |
| u_s | 4.381e-4 | 2.039e-3 | 2.313e-2 | 5.169e-1 | 9.166e-1 | 7.774e-1 |
| v_s | 4.381e-4 | 2.039e-3 | 2.313e-2 | 5.169e-1 | 9.166e-1 | 7.774e-1 |

solution is relatively smooth (differences should only emerge between the two methods in the presence of discontinuities). For comparison, we report the values of the DG normalized error norms in Table 4. We will show DG results on non-conforming grids with static refinement in Sec. 5.3.

In Fig. 9 we plot the time evolution of $\|\phi\|_{L_2}$ during 6 days for 100000 point grids. After the gravity wave adjustment during the first 6 hours (see Galewsky *et al.* (2004)), the regularity of the grid geometry still plays an important role in the evolution of the error even at a resolution that, in global mode, is typically considered fairly high in an operational setting.

So far, the viscous term in the equations has been ignored (i.e. $\delta = 0$). In the quest of diminishing the negative effects of the low resolution on certain grids, we turned viscosity

Table 4. *Equilibrium*. As in table 2, but using DG.

| DG, L_2 | 0.625° | 1.25° | 2.5° | 5.0° |
|------------|---------------|--------------|-------------|-------------|
| RLL | 0.625° | 1.25° | 2.5° | 5.0° |
| N points | 180000 | 49000 | 16000 | 3000 |
| ϕ | 1.384e-8 | 6.556e-7 | 1.203e-4 | 2.151e-3 |
| u_s | 2.189e-5 | 3.261e-4 | 2.636e-2 | 4.794e-1 |
| v_s | 2.189e-5 | 3.260e-4 | 2.640e-2 | 4.794e-1 |
| Hex | 0.625° | 1.25° | 2.5° | 5.0° |
| N points | 124000 | 31000 | 9600 | 1500 |
| ϕ | 6.649e-5 | 4.948e-3 | 6.397e-3 | 1.540e-2 |
| u_s | 7.291e-3 | 4.933e-1 | 4.972e-1 | 9.369e-1 |
| v_s | 7.291e-3 | 4.933e-1 | 4.972e-1 | 9.369e-1 |

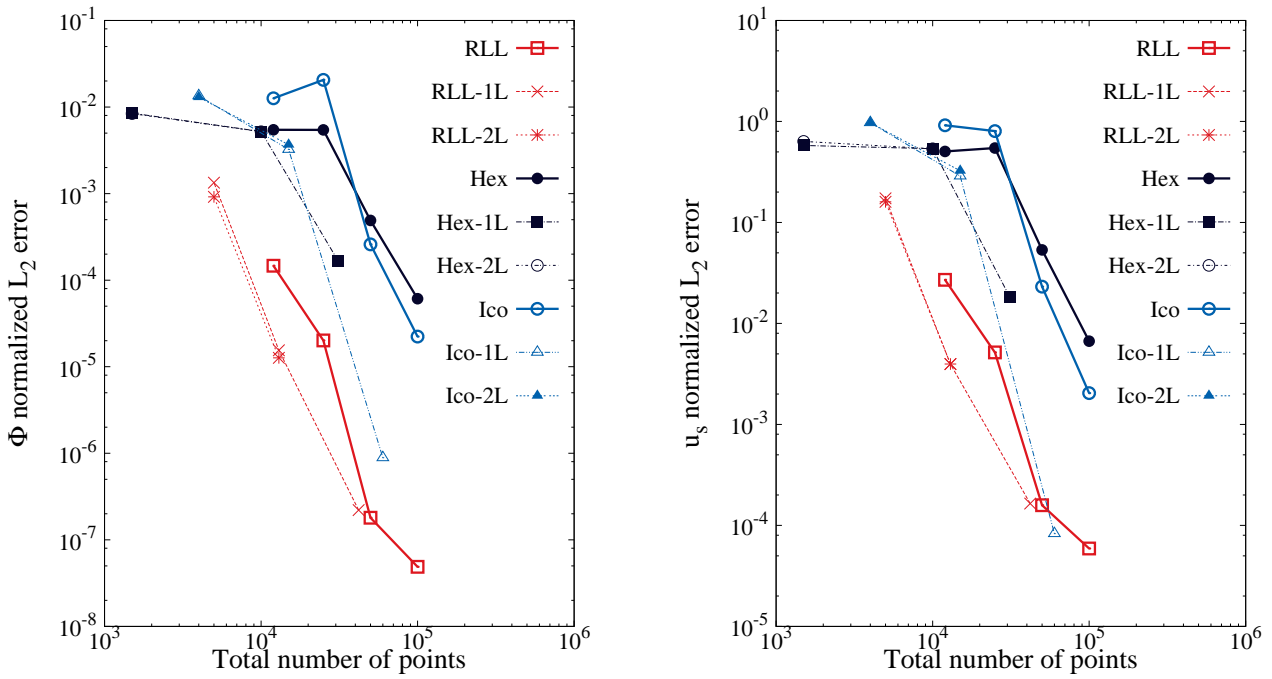


Figure 7. Equilibrium at day 6: Normalized L_2 error norm of ϕ (left) and u_s (right) against the number of grid points. The error is computed with respect to the initial condition of the balanced problem on every grid.

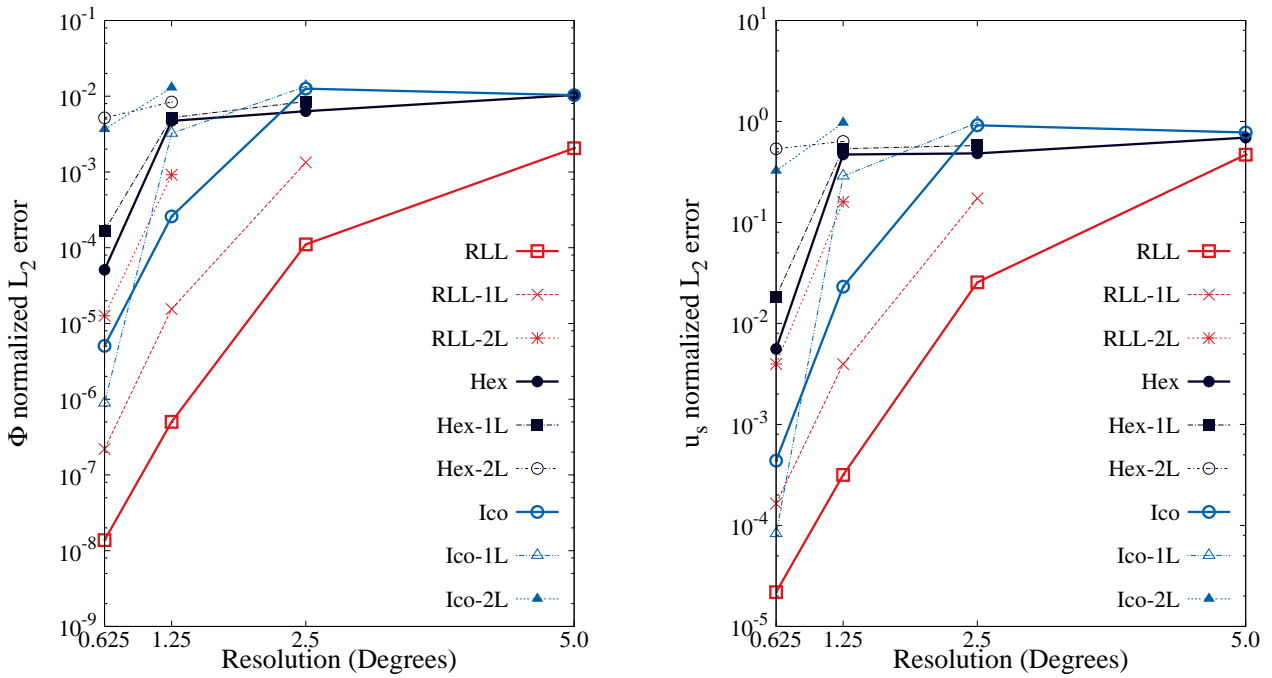


Figure 8. Equilibrium at day 6: Normalized L_2 error norm of ϕ (left) and u_s (right) against the resolution measured in degrees for the RLL and Hex grids. The error is computed with respect to the initial condition of the balanced problem on every grid.

on and recomputed the normalized L_2 error norms that we report in Table 5. We compare these errors against the inviscid estimates using 12000 and 25000 grid points and point out the instances when artificial viscosity was either beneficial or harmful to the error measure. To interpret these values, we need to take a parallel look at the contour plots of Figures 10 and 11. In the case of RLL, where the grid is aligned with the characteristic flow, it was shown above that the resolution does not significantly affect the solution. The opposite, however, occurs in the case of the other two grids. By adding viscosity, what was a bad inviscid solution seems to improve (see the flow pattern after 6 days in Figs. 10, 11, and the error measure in Table 5); in contrast, the solution

that was well behaved in the inviscid case has deteriorated. This behavior is expected for two main reasons: (1) the viscous and inviscid equations are, mathematically, not the same set of equations, and physically represent two different dynamics; (2) viscosity is so large that it is damping all of the modes triggered by the grid on the one hand but, in the same way, damps the solution also where it should not. A thorough analysis of the diffusion mechanisms that are currently used in atmospheric problems goes beyond the scope of this paper. Nevertheless, it should be emphasized that using an arbitrary diffusion operator may not actually improve the solution quality even though the final solution may appear smooth, as we have shown for the RLL grid. This simple result

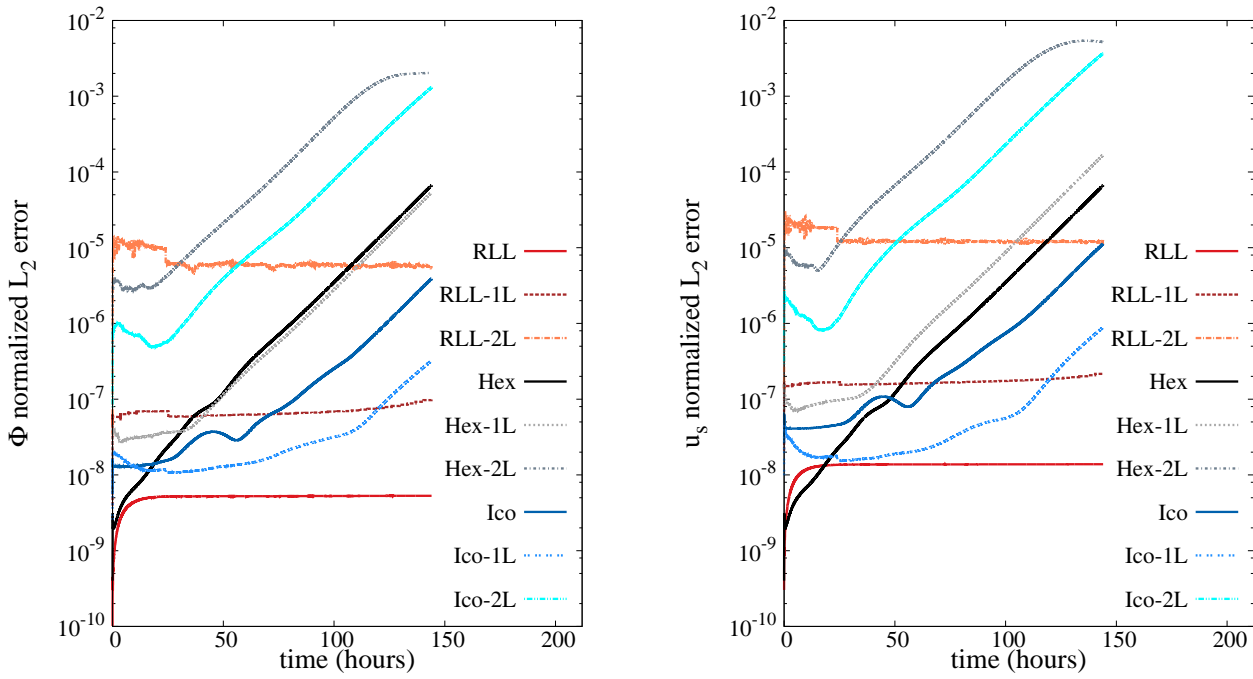


Figure 9. Equilibrium: time evolution of the normalized L_2 error norm of ϕ (left) and u_s (right) relative to the initial condition computed on 100000 grid points.

Table 5. Equilibrium: viscous vs. inviscid solution. Normalized L_2 error norms of (ϕ, u_s, v_s) at day 6 using CG with artificial viscosity (V) $\nu = 1 \times 10^{-5} \text{ m}^2 \text{ s}^{-1}$ on 12000 and 25000 grid points. For a direct comparison, the inviscid (I) errors computed on the same grids are also reported. value indicates that the use of viscosity induced an error increase in the solution. On the contrary, value indicates that the error norm decreased by using viscosity.

| CG, L_2 | | | | |
|------------|-----------------|----------|-----------------|----------|
| N points | 12000-V | 12000-I | 25000-V | 25000-I |
| RLL | | | | |
| ϕ | <u>1.493e-3</u> | 1.466e-4 | <u>1.481e-3</u> | 2.011e-5 |
| u_s | <u>1.575e-1</u> | 2.701e-2 | <u>1.548e-1</u> | 5.162e-3 |
| v_s | <u>1.575e-1</u> | 2.706e-2 | <u>1.548e-1</u> | 5.167e-3 |
| Hex | | | | |
| ϕ | 3.490e-3 | 5.460e-3 | 1.744e-3 | 5.440e-3 |
| u_s | 3.171e-1 | 5.059e-1 | 1.814e-1 | 5.458e-1 |
| v_s | 3.172e-1 | 5.059e-1 | 1.815e-1 | 5.458e-1 |
| Ico | | | | |
| ϕ | 7.002e-3 | 1.263e-2 | 3.284e-3 | 1.057e-2 |
| u_s | 5.762e-1 | 9.163e-1 | 2.947e-1 | 8.035e-1 |
| v_s | 5.762e-1 | 9.163e-1 | 2.947e-1 | 8.035e-1 |

stresses the importance of deriving a proper solution-based stabilization mechanism; we are working on this topic and hope to report our results in a future publication.

5.2. Barotropic instability

Unlike the equilibrium problem, we do not have an analytic solution for the perturbed jet. Because of this, the solution at the highest resolution $\Delta\lambda = 0.625^\circ$ was considered the reference to compute the normalized errors. At this resolution, the RLL reference solution consists of 180000 grid points. Based on the analysis of the equilibrium test and the high sensitivity to the resolution in the case of the hexahedral and icosahedral grids, we considered the high resolution RLL run to be the true solution against which the comparison should be performed. It is a choice that is also supported by the fact that the difference between

the RLL and Hex solutions first, between the Hex and Ico solutions then, and finally between the solutions on the RLL and Ico grids, are of the same order of magnitude (approximately $\Lambda = O(10^{-5} \text{ s}^{-1})$). This makes us confident that the comparison with respect to the RLL will not be biased. After 6 days, the instability has fully developed. The vorticity computed at high resolution is plotted in Fig. 12.

There is no visible difference among the three solutions with $\Delta\varphi \approx 0.625^\circ$. However, as the resolution is decreased, its effect is much more aggressive in the case of the cubed sphere and icosahedron using 12000 and 25000 grid points than it is for RLL. In Figs. 13 and 14, the structure of the jet in the unperturbed region remains regular on the reduced Lat-Lon grid, with a limited effect onto the fully developed jet. For the other two grids to resolve the jet properly, more than 25000 grid points are necessary, as shown in the comparative Fig. 15, where the solutions show little to no difference starting at 50k points when viscosity is turned off.

In Fig. 16, we plot the normalized error norms computed against the total number of grid points. Unlike for the equilibrium case, the error measures of this problem are very similar for the three different grids. This is expected because of the highly irregular structure of the jet which is no longer aligned with any grid. As the resolution is coarsened, the error is sensibly higher than its equilibrium counterpart. What can make the difference in the choice of the grid in this case, may be as simple as selecting the proper number of grid points that keep the error below a certain threshold. At the coarsest resolution, this is most effectively achieved by the RLL grid.

We proceed by testing the implementation for nonconforming grids with static mesh refinement in the section that follows.

5.3. Non-conforming grids

To test the DG solver on nonconforming grids, we defined a statically refined region in the proximity of the zonal

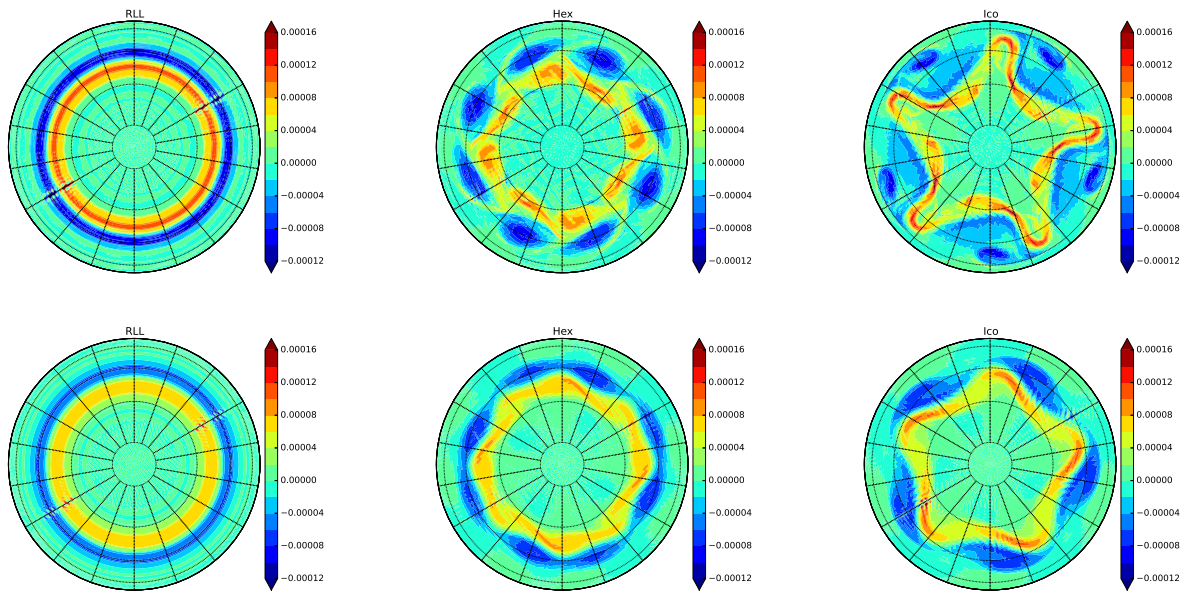


Figure 10. Equilibrium 12000: Vorticity field at day 6. Top row: inviscid solution. Bottom row: artificial diffusion with $\nu = 1 \times 10^5 \text{ m}^2 \text{ s}^{-1}$. Solution on the RLL (left), Hex (center), and Ico (right) grids.

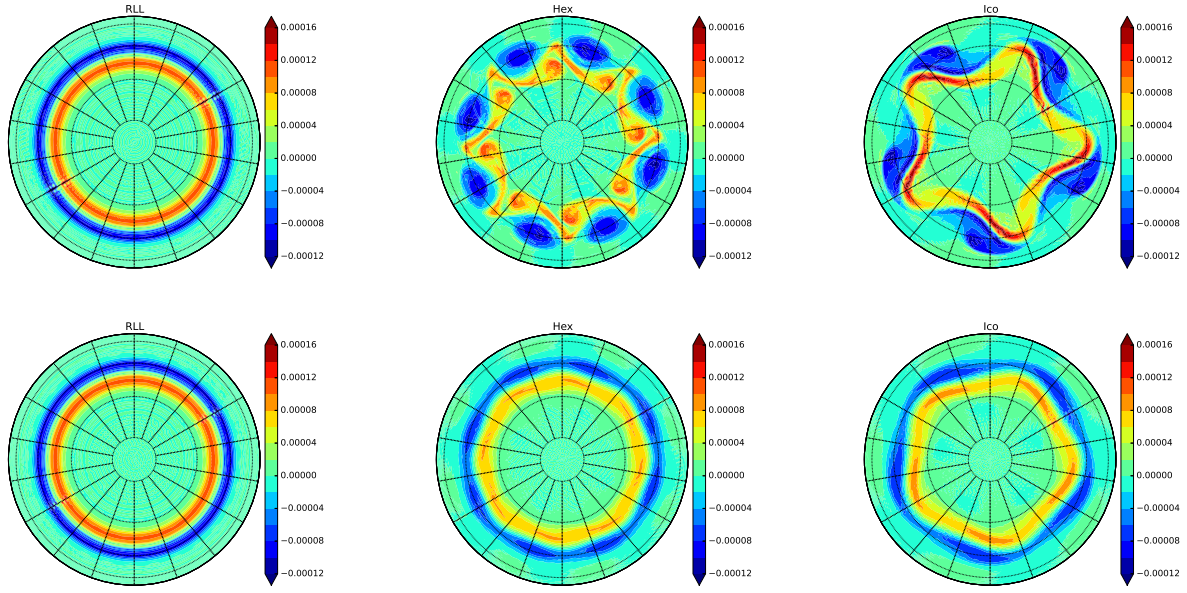


Figure 11. Equilibrium 25k: like Fig. 10, but using 25000 grid points.

wind. The high resolution static refinement was positioned within the latitude band $35^\circ \leq \varphi_{band} \leq 55^\circ$; this region covers approximately 10° above and below the central-line of the initial jet. Similar to the uniform case, we defined a set of different equivalent grid resolutions in the banded region. We used the values in $\Delta\lambda_{band} \approx \Delta\varphi_{band} = \{0.625^\circ, 1.25^\circ, 2.5^\circ\}$. After fixing the resolution in this region, for each grid we added a 1-level and a 2-level global (de-)refinement. The total number of grid points in the global mesh is thus reduced. The grid structure is such that each refined region has half the resolution of its neighbors. If two refinement levels are used, and $\Delta\lambda = 1.25^\circ$ characterizes the finest portion of the mesh, the resolution furthest away from it has a $\Delta\lambda = 5.0^\circ$. Based on the errors on the coarse conforming grids, we did not go beyond this value anywhere in the domain. A total of 6 non-conforming grids were generated and are shown in Fig. 17.

It is well known that the fundamental advantage of adaptive grids (static and dynamic) is reflected in the lower

computational cost in terms of floating point operations since the number of degrees of freedom of the grid is lower than its uniform counterpart. In Tables 6 and 7 we report the normalized L_2 error norms of (ϕ, u_s, v_s) as a function of the number of points given a certain resolution in the region where most of the dynamics happen. In particular, the errors are computed for one and two refinement levels. With reference to Figs. 7 and 8, we observe that, for every grid, the number of grid points necessary to obtain a certain error is reduced by adopting one level of refinement. We would expect for the same to be true once the grid is further coarsened using two refinement levels, however, this is not the case in this particular instance. Due to the non-linearity of the problem and the motion of the gravity waves across the whole domain during the first hours of the simulation, the effect of the poorly resolved gravity waves in the southern hemisphere is clearly felt by the jet resolved at a finer resolution. Back to the 6 day error evolution (Fig. 9), this is clearly observed at

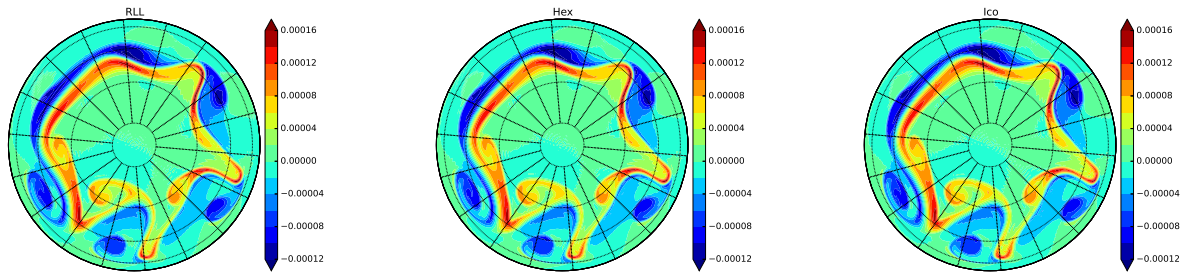


Figure 12. Perturbed jet: vorticity field ($\times 10^{-5} \text{ s}^{-1}$) at day 6. The flow on the RLL grid (left) the Hex (middle), and Ico grid (right) was computed with $\Delta\varphi \approx 0.625^\circ$.

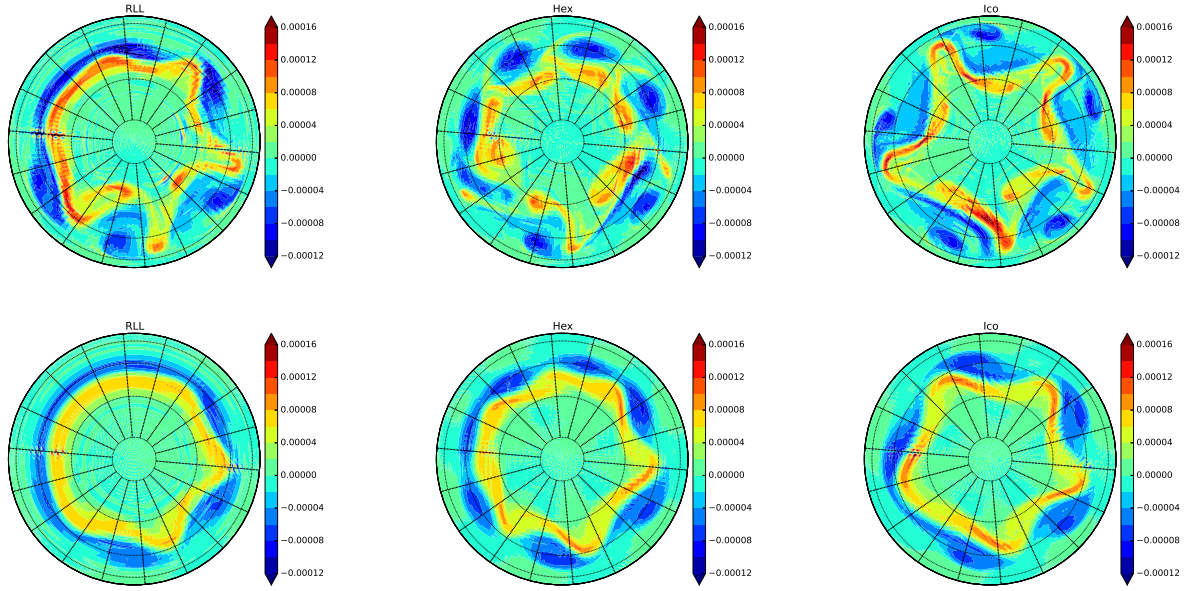


Figure 13. Perturbed jet 12000: vorticity field ($\times 10^{-5} \text{ s}^{-1}$) at day 6. Top row: inviscid solution. Bottom row: with artificial diffusion using $\nu = 1 \times 10^5 \text{ m}^2 \text{ s}^{-1}$. Solution on the RLL (left), Hex (center), and Ico (right) grids.

all times. This issue should not deter us from using more than one level of refinement in general; it simply confirms the well known fact that the criterion for grid adaptation should be very well matched with the problem at hand across the entire domain. For a more thorough analysis of the the construction of DG for non-conforming grids, please, refer to the recent paper by Kopera and Giraldo (2013).

6. Conclusions

We analyzed the behavior of two high order Galerkin methods –spectral elements (CG) and discontinuous Galerkin (DG)– to solve the shallow water equations on six types of spherical grids. We adopted both conforming and non-conforming reduced Lat-Lon (RLL), hexahedral (Hex), and icosahedral (Ico) grids. Among others, one advantageous characteristic of element-based Galerkin methods is that they are not constrained by the logical structure of the mesh. As expected, the spectral element and discontinuous Galerkin solutions showed almost equivalent error measures when executed in conforming mode. In the case of non-conforming grids, we only showed the DG results because we have not implemented non-conforming CG on the sphere. However, we expect the results for non-conforming CG to have the same behavior as the non-conforming DG that was shown in this paper.

St-Cyr et al. (2008) compared a CG-based shallow water model on the cubed sphere to a finite volume solver on

Table 6. Equilibrium: normalized L_2 error of (ϕ, u_s, v_s) at day 6 using DG on the non-conforming, banded grids of Fig. 17. The error is computed with respect to the analytical initial fields given by Eqs. (19,20).

| DG 1-level, L_2 | | | |
|-------------------|-------------|-----------|----------|
| RLL-NC | 0.625/1.25° | 1.25/2.5° | 2.5/5.0° |
| N points | 43000 | 13000 | 5000 |
| ϕ | 2.207e-7 | 1.548e-5 | 1.337e-3 |
| u_s | 1.647e-4 | 3.960e-3 | 1.734e-1 |
| v_s | 1.647e-4 | 3.960e-3 | 1.730e-1 |
| Hex-NC | 0.625/1.25° | 1.25/2.5° | 2.5/5.0° |
| N points | 31000 | 10000 | 1500 |
| ϕ | 1.680e-4 | 5.210e-3 | 8.513e-3 |
| u_s | 1.844e-2 | 5.372e-1 | 5.783e-1 |
| v_s | 1.844e-2 | 5.372e-1 | 5.783e-1 |
| Ico-NC | 0.625/1.25° | 1.25/2.5° | 2.5/5.0° |
| N points | 61000 | 15000 | 4000 |
| ϕ | 8.881e-7 | 3.241e-3 | 1.348e-2 |
| u_s | 8.294e-5 | 2.879e-1 | 9.729e-1 |
| v_s | 8.294e-5 | 2.879e-1 | 9.729e-1 |

a Lat-Lon grid. From their study, they concluded that spectral elements are unable to capture the solution at certain resolutions on the cubed sphere. In this paper we showed that the inaccurate CG solution on the cubed sphere is not to be blamed on the numerical method per se, but

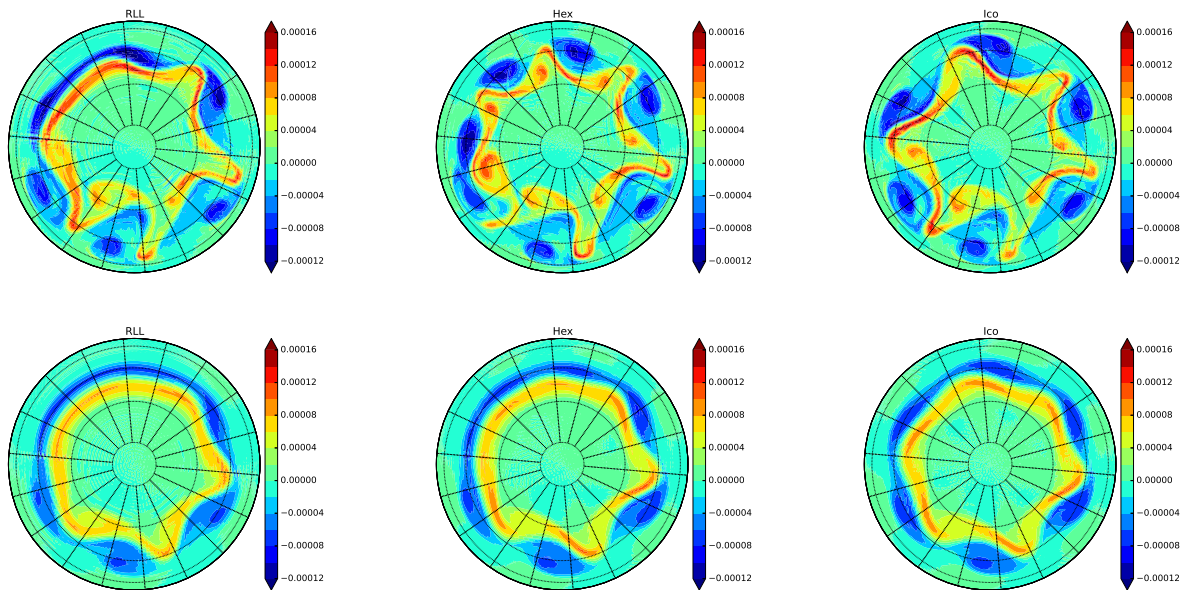


Figure 14. Perturbed jet 25k: like Fig. 13, but with 25000 grid points.

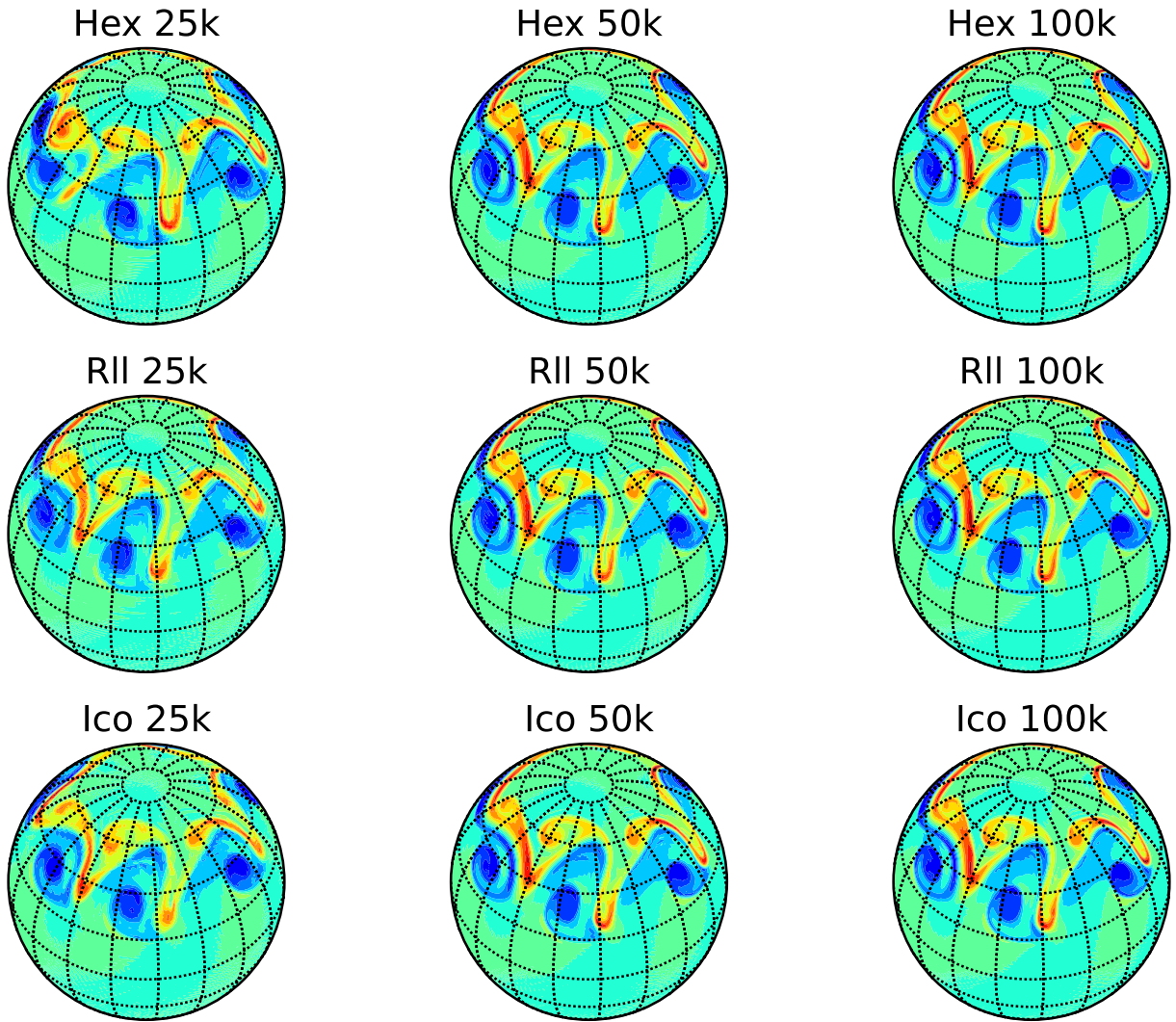


Figure 15. Perturbed jet: vorticity field ($\times 10^{-5} \text{ s}^{-1}$) after 6 days. Top row: Hex. Middle row: RLL. Bottom row: Ico. Solutions plotted for 25000, 50000, and 100000 grid points (from left to right). The color scale ranges between $-12 \times 10^{-5} \text{ s}^{-1}$ (dark blue) and $16 \times 10^{-5} \text{ s}^{-1}$.

rather, on the unfortunate combination of the resolution and mesh alignment with the dynamics of the problem at hand.

We confirmed that a coarse resolution is responsible for the breaking of the solution; however, by a simple change of

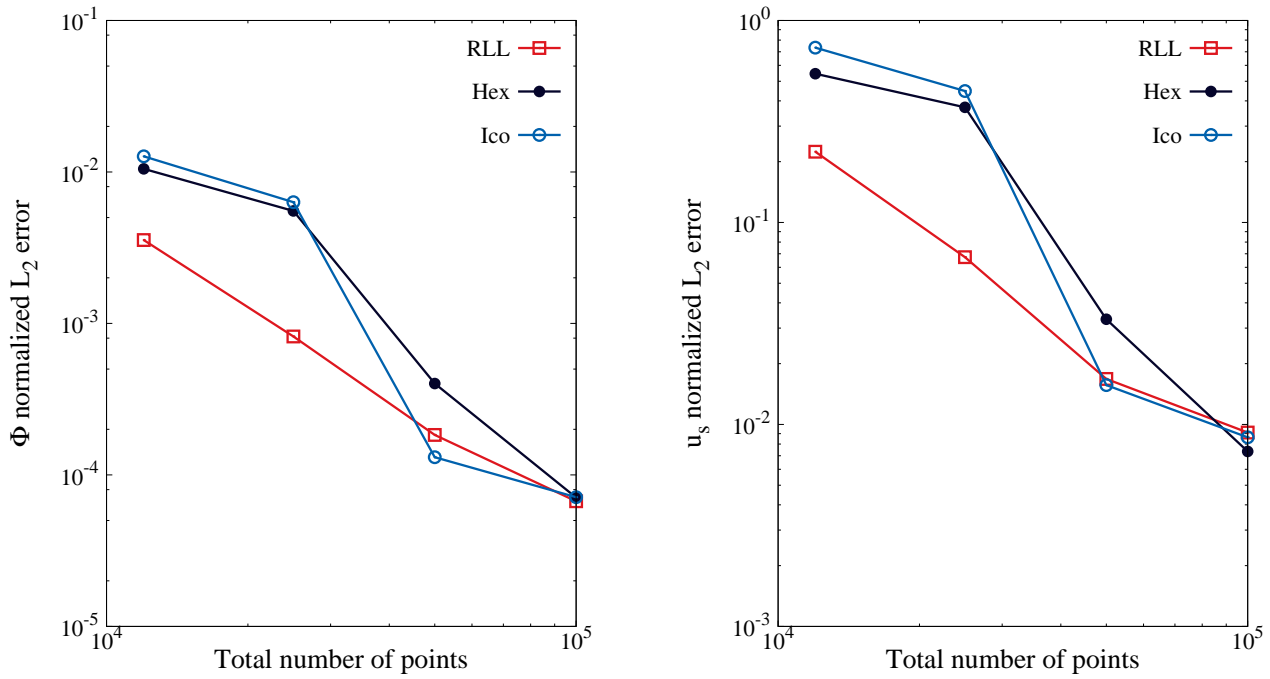


Figure 16. Perturbed jet at day 6: Normalized L_2 error norms of ϕ (left) and u_s (right) against the number of grid points. The error is computed with respect to the 8th order RLL solution at 0.625° , which corresponds to 180000 points.

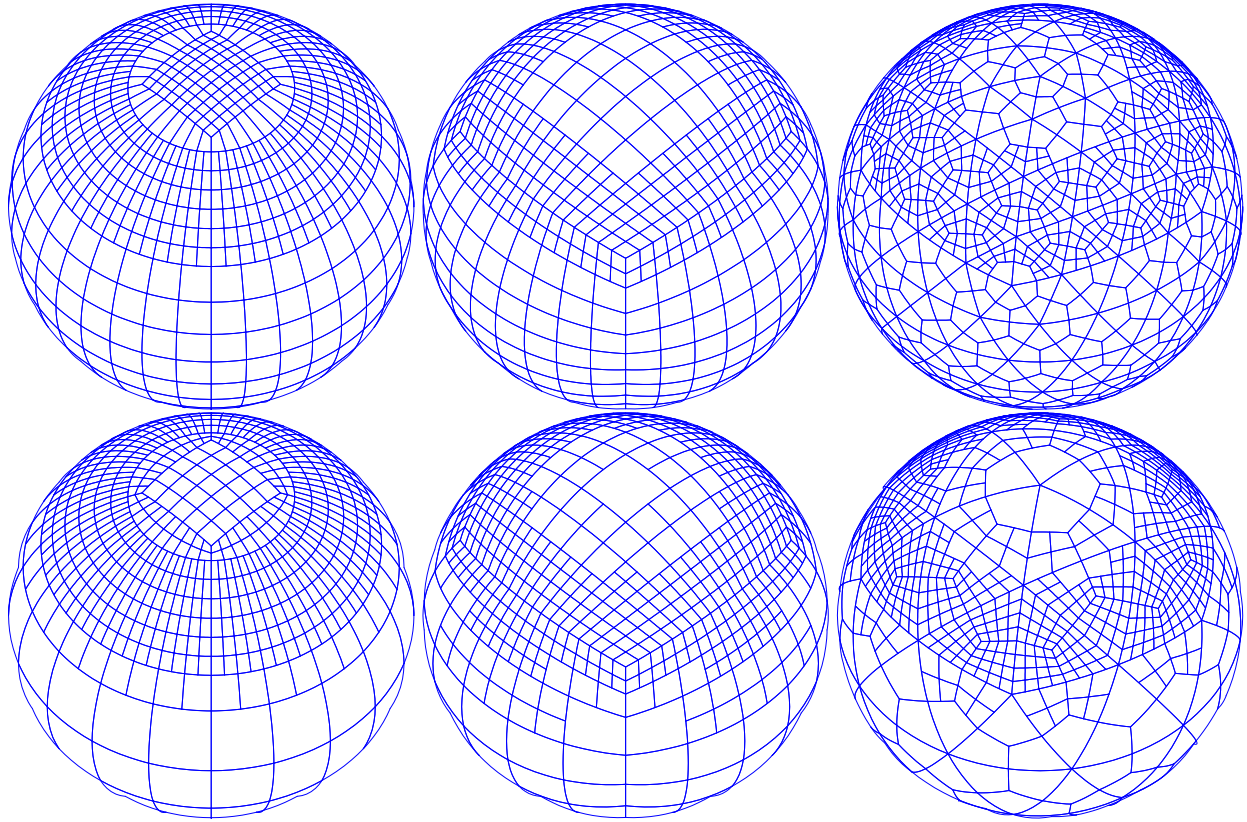


Figure 17. High-order (curved elements) non-conforming grid with 1-level (top row) and 2-level (bottom row) refinements. RLL (left column), Hex (middle column), and Ico (right column). The highest resolution in the main region of interest is $\approx \Delta\varphi = 0.625^\circ$.

the grid geometry, we have disproved the responsibility of CG alone by showing that the instabilities are merely an undesired effect of the grid configuration.

To show the flexibility of high-order spectral elements and discontinuous Galerkin with respect to the mesh, and how the solution may be sensitive to the grid configuration, we used the highly non-linear zonal flow tests proposed by Galewsky *et al.* (2004). Galewsky's tests consist of (i) an unperturbed mid-latitude zonal jet on top of a

geostrophically balanced geopotential height, and (ii) its perturbed counterpart where the perturbation is triggered by a bump in the geopotential.

The first main conclusion from our analysis is that both the inviscid and viscous solutions have shown an important sensitivity to the mesh resolution and geometry. Particularly so are the solutions on the hexa- and ico-sahederal grids at low resolution. We observed the same behavior for both Galewskys's tests. In the case of the flow in equilibrium,

Table 7. As Table 6, but with 2-level refinement.

| DG 2-level, L_2 | | |
|-------------------|-----------------|---------------|
| RLL-NC | 0.625/1.25/2.5° | 1.25/2.5/5.0° |
| N points | 13000 | 5000 |
| ϕ | 1.265e-5 | 9.183e-4 |
| u_s | 3.964e-3 | 1.599e-1 |
| v_s | 3.964e-3 | 1.599e-1 |
| Hex-NC | 0.625/1.25/2.5° | 1.25/2.5/5.0° |
| N points | 9600 | 1500 |
| ϕ | 5.187e-3 | 8.398e-3 |
| u_s | 5.364e-1 | 6.348e-1 |
| v_s | 5.364e-1 | 6.348e-1 |
| Ico-NC | 0.625/1.25/2.5° | 1.25/2.5/5.0° |
| N points | 15000 | 4000 |
| ϕ | 3.670e-3 | 1.298e-2 |
| u_s | 3.249e-1 | 9.695e-1 |
| v_s | 3.249e-1 | 9.695e-1 |

as the resolution is decreased below an approximate value of 1.25° in latitude and longitude, the misalignment of the mesh in the Hex and Ico configurations is fatal. The fact that the grid may not be aligned with the flow (which is likely the case in most real-life simulations) showed not to be the only factor of concern in certain configurations. In fact, although the flow is not aligned with any of the three grids in the case of the barotropically unstable jet, the solution on the reduced Lat-Lon was only slightly affected, whereas the accuracy was completely lost for the other two configurations. We executed the same tests with and without artificial viscosity. Based on the results obtained with the use of artificial viscosity, we believe that the extremely large and unphysical diffusion that was added by means of a second-order Laplace operator with coefficient $\nu = 1 \times 10^5 \text{ m}^2\text{s}^{-1}$, should be avoided for the sake of accuracy.

6.1. Acknowledgements

The authors gratefully acknowledge the support of the Office of Naval Research through program element PE-0602435N, the National Science Foundation (Division of Mathematical Sciences) through program element 121670, and the Air Force Office of Scientific Research through the Computational Mathematics program. The authors would like to acknowledge the Isaac Newton Institute for Mathematical Sciences at Cambridge University, UK, where part of this work was initiated during the workshop *Adaptive Multiscale Methods for the Atmosphere and Ocean*. The inputs by Dr. Hilary Weller (University of Reading, UK) on the issues of grid adaptivity in atmospheric simulations is greatly appreciated. The authors would also like to thank Dr. James F. Kelly (Exa Corp., Burlington, MA, USA) and Dr. Andreas Müller (Naval Postgraduate School) who read the manuscript and gave insightful recommendations. The work of the first and second authors was supported by the National Academies through a National Research Council fellowship.

References

- Behrens J. 2006. *Adaptive atmospheric modeling. Key techniques in grid generation, data structures, and numerical operations with applications*. Springer.
- Boyd J. 1996. The erfc-log filter and the asymptotics of the Euler and Vandeven sequence accelerations. In: *Proc. Third Int. Conf. Spectral and High Order Methods*. Houston Journal of Mathematics, Houston, Texas. pp. 267–276.
- Browning GL, Hack JJ, Swarztrauber PN. 1989. A comparison of three numerical methods for solving differential equations on the sphere. *Mon. Wea. Rev.* **117**: 1058–1075.
- Cockburn B, Shu CW. 2001. Runge-kutta discontinuous Galerkin methods for convection-dominated problems. *J. of Sci. Computing* **16**: 173–261.
- Coté J. 1988. A Lagrange multiplier approach for the metric terms of semi-lagrangian models on the sphere. *Quart. J. Royal Meteor. Soc.* **114**(483): 1347–1352.
- Courant R, Friedrichs K, Lewy H. 1967. On the partial difference equations of mathematical physics. *IBM Journal. English translation from the original article written in German.* **100**: 215–234.
- Eriksson LE. 1984. Transfinite mesh generation and computer-aided analysis of mesh effects. PhD thesis, University of Uppsala, Sweden.
- Gabersk S, Giraldo FX, Doyle J. 2012. Dry and moist idealized experiments with a two-dimensional spectral element model. *Mon. Wea. Rev.* **140**: 3163–3182.
- Galewsky J, Scott R, Polvani L. 2004. An initial-value problem for testing numerical models of the global shallow-water equations. *TELLUS* **56A**: 429–440.
- Giraldo FX. 2001. A spectral element shallow water model on spherical geodesic grids. *Int. J. Num. Meth. Fluids* **35**: 869–901.
- Giraldo FX, Hesthaven JS, Warburton T. 2002. Nodal high-order discontinuous Galerkin methods for spherical shallow water equations. *J. Comput. Phys.* **181**: 499–525.
- Giraldo FX, Kelly JF, Constantinescu E. 2013. Implicit-explicit formulations of a three-dimensional Nonhydrostatic unified model of the atmosphere (NUMA). *SIAM J. Sci. Comput.* **35**.
- Giraldo FX, Warburton T. 2005. A nodal triangle-based spectral element method for the shallow water equations on the sphere. *J. Comput. Phys.* **207**: 129–150.
- Gordon WN, Hall CA. 1973. Construction of curvilinear coordinate systems and application to mesh generation. *Int. J. Numer. Methods Engrg.* **7**: 461–477.
- Hogan T, Rosmond T, Gelaro R. 1991. The nogaps forecast model: A technical description. Technical Report ADA247216, Naval Oceanographic and Atmospheric Research Lab. Monterey, CA. U.S.A.
- Kelly JF, Giraldo FX. 2012. Continuous and discontinuous Galerkin methods for a scalable three-dimensional nonhydrostatic atmospheric model: Limited-area mode. *J. Comput. Phys.* **231**: 7988–8008.
- Kopera MA, Giraldo FX. 2013. Analysis of adaptive mesh refinement for IMEX discontinuous Galerkin solutions of the compressible Euler equations with application to atmospheric simulations. *Submitted to J. Comput. Phys.* .
- Lanser D, Blom JG, Verwer JG. 2000. Spatial discretization of the shallow water equations in spherical geometry using Osher's scheme. *J. Comput. Phys.* **165**: 542–565.
- Malm J, Schlatter P, Fischer PF, Henningson DS. 2013. Stabilization of the spectral element method in convection dominated flows by recovery of skew-symmetry. *J. Sci. Comput.* **57**: 254–277.
- Marras S, Moragues M, Vázquez MR, Jorba O, Houzaux G. 2013a. Simulations of moist convection by a variational multiscale stabilized finite element method. *J. Comput. Phys.* **252**: 195–218.
- Marras S, Moragues M, Vázquez MR, Jorba O, Houzaux G. 2013b. A variational multiscale stabilized finite element method for the solution of the Euler equations of nonhydrostatic stratified flows. *J. Comput. Phys.* **236**: 380–407.
- Müller A, Behrens J, Giraldo FX, Wirth V. 2013. Comparison between adaptive and uniform discontinuous Galerkin simulations in dry 2D bubble experiments. *J. Comput. Phys.* **235**: 371–393.
- Nair RD, Thomas SJ, Loft RD. 2007. A discontinuous Galerkin global shallow water model. *Mon. Wea. Rev.* **133**.
- Peixoto PS, Barros SR. 2013. Analysis of grid imprinting on geodesic icosahedral grids. *J. of Comput. Phys.* **237**: 61–78.
- Phillips N. 1957. A map projection system suitable for large-scale numerical weather prediction. *J. Meteor. Soc. Japan* **75**: 262–267.
- Qaddouri A, Pudykiewicz J, Tanguay M, Girard C, Coté J. 2012. Experiments with different discretizations for the shallow-water equations on a sphere. *Quart. J. Royal Meteor. Soc.* **138**: 989–1003.
- Ronchi C, Iacono R, Paolucci PS. 1996. The Cubed Sphere: a new method for the solution of partial differential equations in

- spherical geometry. *J. Comput. Phys.* **124**: 93–114.
- Sadourny R. 1972. Conservative finite-difference approximations of the primitive equations on quasi-uniform spherical grids. *Mon. Wea. Rev.* **100**(2): 136–144.
- Sadourny R, Arakawa A, Mintz Y. 1968. Integration of the non-divergent barotropic vorticity equation with an icosahedral-hexagonal grid for the sphere. *Mon. Wea. Rev.* **96**: 351–356.
- Song C, Wolf JP. 1999. The scaled boundary finite element method –alias consistent infinitesimal finite element cell method– for diffusion. *Int. J. Numer. Methods Engrg.* **45**: 1403–1431.
- Spiteri RJ, Ruuth SJ. 2002. A new class of optimal high-order strong-stability-preserving time discretization methods. *SIAM J. Numer. Anal.* **40**: 469–491.
- St-Cyr A, Jablonowski C, Dennis JM, Tufo HM, Thomas SJ. 2008. A comparison of two shallow-water models with nonconforming adaptive grids. *Mon. Wea. Rev.* : 1898–1922.
- Staniforth A, Thuburn J. 2012. Horizontal grids for global weather and climate prediction models: a review. *Quart. J. Royal Meteor. Soc.* **138**: 1–26.
- Starius G. 1977. Composite mesh difference methods for elliptic and boundary value problems. *Numer. Math.* **28**: 243–258.
- Taylor MA, Overfelt JR, Levy M. 2013. A variable resolution spectral element dynamical core in the Community Atmosphere Model. Technical Report 2013-0697J, Sandia National Laboratories.
- Taylor MA, Tribbia J, Iskandarani M. 1997. The spectral element method for the shallow water equations on the sphere. *J. Comput. Phys.* **130**: 92–108.
- Thompson JF. 1987. A general three dimensional elliptic grid generation system on a composite block-structure. *Comput. Methods Appl. Mech. Engrg.* **64**: 377–411.
- Weller H, Thuburn J, Cotter CJ. 2012. Computational modes and grid imprinting on five quasi-uniform spherical C grids. *Mon. Wea. Rev.* **140**: 2734–2755.
- Williamson D, Drake J, Hack J, Jakob R, Swartztrauber P. 1992. A standard test set for numerical approximations to the shallow water equations in spherical geometry. *J. Comput. Phys.* **102**: 211–224.